

Journal of Geophysical Research: Atmospheres

RESEARCH ARTICLE

10.1002/2017JD027916

Key Points:

- Observed PPHB in MBL cloud scenes can be larger than 5 for cloud optical thickness, several microns for effective droplet radius
- Mathematical framework can explain and correct for observed PPHB
- PPHB correction still yields reliable results if only a few subpixels or just a single visible band provides high-resolution reflectances

Correspondence to:F. Werner,
frankw@umbc.edu**Citation:**

Werner, F., Zhang, Z., Wind, G., Miller, D. J., & Platnick, S. (2018). Quantifying the impacts of subpixel reflectance variability on cloud optical thickness and effective radius retrievals based on high-resolution ASTER observations. *Journal of Geophysical Research: Atmospheres*, 123, 4239–4258.
<https://doi.org/10.1002/2017JD027916>

Received 18 OCT 2017

Accepted 15 MAR 2018

Accepted article online 30 MAR 2018

Published online 26 APR 2018

Quantifying the Impacts of Subpixel Reflectance Variability on Cloud Optical Thickness and Effective Radius Retrievals Based On High-Resolution ASTER Observations

F. Werner¹ , Z. Zhang² , G. Wind³ , D. J. Miller² , and S. Platnick³ 

¹Joint Center for Earth Systems Technology, Baltimore, MD, USA, ²Physics Department, University of Maryland, Baltimore, MD, USA, ³NASA Goddard Space Flight Center, Greenbelt, MD, USA

Abstract Recently, Zhang et al. (2016, <https://doi.org/10.1002/2016JD024837>) presented a mathematical framework based on a second-order Taylor series expansion in order to quantify the plane-parallel homogeneous bias (PPHB) in cloud optical thickness (τ) and effective droplet radius (r_{eff}) retrieved from the bispectral solar reflective method. This study provides observational validation of the aforementioned framework, using high-resolution reflectance observations from the Advanced Spaceborne Thermal Emission and Reflection Radiometer (ASTER) over 48 marine boundary layer cloud scenes. ASTER reflectances at a horizontal resolution of 30 m are aggregated up to a scale of 1,920 m, providing retrievals of τ and r_{eff} at different spatial resolutions. A comparison between the PPHB derived from these retrievals and the predicted PPHB from the mathematical framework reveals a good agreement with correlation coefficients of $r > 0.97$ (for $\Delta\tau$) and $r > 0.79$ (for Δr_{eff}). To test the feasibility of PPHB predictions for present and future satellite missions, a scale analysis with varying horizontal resolutions of the subpixel and pixel-level observations is performed, followed by tests of corrections with only limited observational high-resolution data. It is shown that for reasonably thick clouds with a mean subpixel τ larger than 5, correlations between observed and predicted PPHB remain high, even if the number of available subpixels decreases or just a single band provides the information about subpixel reflectance variability. Only for thin clouds the predicted Δr_{eff} become less reliable, which can be attributed primarily to an increased retrieval uncertainty for r_{eff} .

Plain Language Summary Assumptions in the retrieval of cloud optical and microphysical properties from remote sensing observations can be substantially biased. Only recently, we gained a better understanding of these biases, aided by a mathematical framework that makes use of the subpixel variability within an observed pixel. This study uses novel satellite observations at a very high resolution to provide observational validation of the proposed mathematical framework, which before was mainly tested on a single synthetic cloud field based on simulations. The presented results illustrate that the mathematical framework can reliably correct for the observed bias. Moreover, this approach also yields reasonable results when applied to more common satellite setup, which are usually characterized by lower spatial resolutions or limited availability of subpixel observations.

1. Introduction

One of the most widely used passive cloud property remote sensing techniques is the so-called bispectral solar reflectance method, where cloud-top reflectances (R) at two different wavelengths are used to simultaneously infer the cloud optical thickness (τ) and effective droplet radius (r_{eff}) (Nakajima & King, 1990; Nakajima et al., 1991; Twomey & Seton, 1980). Reflectances at one wavelength are usually sampled in the visible to near-infrared spectral wavelength range (VNIR), where scattering is dominant and R increases with increasing τ . Conversely, reflectances at the second wavelength are sampled in a dominant bulkwater-absorption band in the shortwave-infrared spectral wavelength range (SWIR), where R typically decreases with increasing r_{eff} . The relationships between the cloud variables and the two reflectances R_V and R_S (in the VNIR and SWIR, respectively) are usually precomputed for a wide range of possible τ and r_{eff} combinations, as well as different solar and viewing geometries, in so-called lookup tables (LUT). Subsequently, multidimensional interpolation within the respective LUT yields retrieved τ and r_{eff} for each R_V and R_S pair. Global estimates of τ and r_{eff}

by means of the bispectral solar reflective method are provided by a multitude of past and present satellite missions, such as Landsat Nakajima et al. (1991), the Moderate Resolution Imaging Spectroradiometer (MODIS, Platnick et al., 2003), the Visible Infrared Imaging Radiometer Suite (VIIRS, Lee et al., 2006; Walther et al., 2013), and the Spinning Enhanced Visible and Infrared Imager (SEVIRI, Roebeling et al., 2006).

Retrievals using the bispectral solar reflective method rely on a number of critical assumptions. Of particular interest of this study is the assumption that clouds within a cloudy pixel are horizontally homogeneous and their reflectance is interpreted on the basis of one-dimensional (1-D) plane-parallel radiative transfer. Because in the 1-D plane-parallel model there is no net horizontal photon transport between individual pixels within a scene, this approach is called the independent pixel approximation (IPA, see Cahalan, Ridgway, Wiscombe, & Bell, 1994; Cahalan, Ridgway, Wiscombe, Gollmer, & Harshvardhan, 1994). By applying 1-D radiative transfer to three-dimensional (3-D) cloud structures, the IPA introduces two general 3-D radiative effects. For observations with a high spatial resolution the resolved horizontal scales are well below the free photon length path observed in the atmosphere. For such observations, ignoring horizontal photon transport between cloudy columns yields a breakdown of IPA, which was illustrated by scale breaks in the power spectral densities of cloud-top reflectances (Davis et al., 1997; Marshak et al., 1995; Oreopoulos et al., 2000), as well as by increased uncertainties in retrieved τ (Barker & Liu, 1995; Chambers et al., 1997). In contrast, for observations with a low spatial resolution the assumption of horizontally homogeneous cloud structures within a pixel is likely no longer valid. As a result, IPA introduces large uncertainties in the pixel-level τ and r_{eff} retrievals if these cloud variables change on the unresolved subpixel scale. This is especially true for very inhomogeneous cloud fields, consisting of precipitating clouds or broken cumulus (Di Girolamo et al., 2010; Liang et al., 2015; Painemal & Zuidema, 2011). Marine low-level clouds are especially susceptible to changes in aerosol loading and accurate retrievals of r_{eff} are essential in assessing aerosol-cloud interactions on regional and global scales (Werner et al., 2014; Wood et al., 2016).

Studies by Cahalan, Ridgway, Wiscombe, and Bell (1994) and Marshak et al. (2006) on unresolved variability discussed biases in retrieved τ and r_{eff} , which are caused by the nonlinear relationship between the cloud variables and the cloud-top reflectances R_V and R_S . These studies demonstrated an inequality between the reflectances and retrievals on the pixel-level scale and the mean values of the higher-resolution subpixel results. This inequality is called the plane-parallel homogeneous bias (PPHB). One of the considerations in past studies was that the PPHB for τ is only a function of R_V , while the PPHB for r_{eff} is only determined by the behavior of R_S . Lately, Zhang and Platnick (2011) and Zhang et al. (2012) discussed the bias contributions from the codependence of the τ and r_{eff} retrievals due to the fact that the respective isolines in the LUT are not orthogonal. A unified framework was introduced in Zhang et al. (2016, hereafter Z16), which acknowledges the fact that τ and r_{eff} are functions of both R_V and R_S . That study used a second-order Taylor series expansion of τ and r_{eff} with respect to both reflectances to illustrate that the PPHB can be predicted from the knowledge of subpixel reflectance variability.

For present and future satellite missions the Z16 study is significant, as it provides a comprehensive mathematical explanation for the impact of unresolved cloud variability on cloud property retrievals at different horizontal scales. For example, observed biases due to plane-parallel assumptions in the operational MODIS retrievals (performed at 1,000-m horizontal resolution) could be mitigated by correcting the retrieved pixel-level cloud properties. This correction would be based on predicted PPHB values, which are derived from sampled VNIR and SWIR reflectances at 500 m. This would yield pixel-level retrievals that are close to the subpixel averages of the respective cloud products, by simultaneously avoiding the practical limitations high-resolution τ and r_{eff} retrievals would impose (e.g., increased computational costs and file sizes). However, numerical tests presented in Z16 were mainly based on synthetic marine boundary layer (MBL) cloud fields generated by large eddy simulations. Correlations between actually observed and predicted PPHB for an example MODIS scene were slightly lower and especially for optically thin clouds the prediction seemed to be less reliable. Clearly, more extensive experimental validation of the prediction framework is necessary.

This is a follow-up study to Z16, which aims to further evaluate the mathematical framework with high-resolution Advanced Spaceborne Thermal Emission and Reflection Radiometer (ASTER) observations of 48 inhomogeneous MBL scenes. A newly developed, ASTER-specific retrieval algorithm provides retrievals of τ and r_{eff} at a horizontal resolution of 30 m Werner et al. (2016). This data set allows for an extensive test of the PPHB prediction scheme introduced in Z16, as well as a sensitivity study with different horizontal resolutions. The manuscript is structured as follows: an overview of ASTER observations and the retrieval algorithm

is given in section 2. A description of the PPHB, as well as the mathematical framework to predict the biases in τ and r_{eff} , is presented in section 3. The prediction framework is applied to high-resolution ASTER data in order to mitigate the observed PPHB, first in a case study in section 4.1, and subsequently for all 48 MBL scenes in section 4.2. To test the practical implementation of the mathematical framework for present and future satellite missions, a scale analysis for different horizontal resolutions of the subpixel and pixel-level data, followed by a feasibility study of a correction based on just a single band, is presented in section 5. A summary is given in section 6.

2. ASTER Observations

Data in this study are provided by high-resolution ASTER observations over the 48 MBL scenes detailed in Werner et al. (2016). These observations are composed of selected altocumulus and broken cumulus scenes, which were sampled off the coast of California. They are characterized by a wide range of possible τ and r_{eff} solutions, different scene cloud covers, and varying solar zenith angles.

Detailed information on ASTER are provided by Yamaguchi and Hiroji (1993), Yamaguchi et al. (1998), and Abrams (2000). ASTER samples in the VNIR are characterized by a spatial resolution of 15 m, increasing to 30 and 90 m in the SWIR and thermal infrared spectral wavelength range, respectively. Applying the equations and coefficients reported in Abrams et al. (2004) on the raw digital ASTER counts yields ASTER cloud-top reflectances with absolute radiometric uncertainties of <4% (Yamaguchi et al., 1998).

Retrievals of τ and r_{eff} are facilitated by the ASTER-specific, research-level retrieval algorithm presented in Werner et al. (2016), which utilizes the same algorithms as the operational MODIS C6 retrievals (King et al., 1997; Platnick et al., 2003). The use of this well-tested and documented algorithm setup provides reliable results for cloud-top, optical, and microphysical variables based on ASTER observations, which compare well with the operational MODIS C6 products (Werner et al., 2016). The mean retrieval uncertainties are 15% for τ and 23% for r_{eff} . Although the ASTER reflectance samples in the VNIR have a higher horizontal resolution, the bispectral retrieval approach utilizes R observations in both the VNIR and SWIR, respectively. Thus, the highest spatial resolution of R , τ , and r_{eff} provided by ASTER measurements is 30 m. Aggregation of measured R at 30 m within larger pixels, in combination with MODIS-like retrievals based on the ASTER-specific retrieval algorithm, provides retrievals of τ and r_{eff} for a wide range of horizontal resolutions. In this study pixel sizes are varied between 30 and 1,920 m, spanning the range of native ASTER resolution to scales larger than the operational MODIS cloud property retrievals.

From here on R_V indicates the ASTER band 3N (nadir-viewing mode) reflectance centered around a wavelength of $\lambda = 0.86 \mu\text{m}$ (in the VNIR), while R_S identifies the ASTER band 5 reflectance centered around $\lambda = 2.1 \mu\text{m}$ (in the SWIR).

3. PPHB and Prediction Framework

This section gives a short introduction to the PPHB for τ and r_{eff} retrievals by means of a case study. Subsequently, a brief summary of the mathematical framework for the PPHB decomposition and prediction, first reported in Z16, is given. Finally, issues in the definition of the PPHB and the prediction framework for partially cloudy (PCL) pixels are discussed.

3.1. Plane-Parallel Homogeneous Bias

Figure 1 shows an example LUT composed of precomputed R_V and R_S . The solar zenith angle is $\theta_0 = 48.7^\circ$, while the relative azimuth angle (related to the difference between sensor and solar azimuth angle), and sensor zenith angle are close to 0° . This geometry represents ASTER observations on 2 March 2006 at 19:14:44 UTC (case C1 in Werner et al., 2016).

From the shape of the LUT it can be seen that τ and r_{eff} vary mostly with R_V and R_S , respectively. However, the curvatures in the τ and r_{eff} isolines reveal the nonlinear relationship between cloud variables and cloud-top reflectances, which define the contributions to the total PPHB that were discussed in Cahalan, Ridgway, Wiscombe, and Bell (1994) and Marshak et al. (2006). It is also obvious that τ isolines are not orthogonal to the r_{eff} isolines, which indicates that reflectances in the VNIR and SWIR covary with τ and r_{eff} . In turn, this means that retrievals of both parameters are not independent from one another. This effect contributes to the total PPHB (Zhang & Platnick, 2011; Zhang et al., 2012).

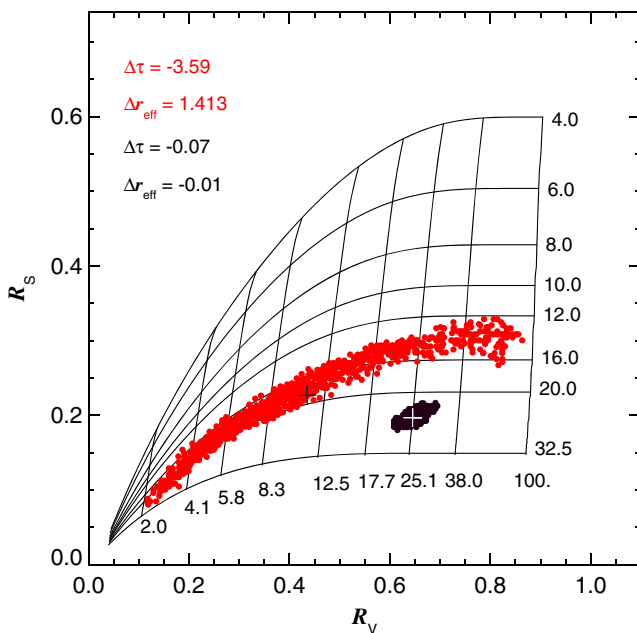


Figure 1. Example lookup table from Advanced Spaceborne Thermal Emission and Reflection Radiometer band 3N reflectances (R_V) in the visible to near-infrared spectral wavelength range and band 5 reflectances (R_S) in the SWIR. Black and red circles indicate Advanced Spaceborne Thermal Emission and Reflection Radiometer measurements for two pixels: one with low and the other with high subpixel reflectance variability, respectively. The black (white) plus sign indicates the mean value of subpixel reflectances for the more inhomogeneous (homogeneous) example pixel.

The black dots in Figure 1 illustrate 1,024 samples of R_V and R_S at 30-m horizontal resolution within a larger pixel with a horizontal resolution of 960 m (i.e., a MODIS-like horizontal resolution). This example indicates a pixel containing a rather homogeneous cloud, where there is little variability in R_V and R_S and all data points are grouped closely together. The subpixel cloud variability can be quantified by calculating the inhomogeneity index $H_{\sigma,V}$:

$$H_{\sigma,V} = \frac{\sigma_V}{\bar{R}_V}, \quad (1)$$

which is defined as the ratio of spatial standard deviation (σ_V) to mean value (\bar{R}_V , indicated by the horizontal bar) of the subpixel VNIR reflectance (Cho et al., 2015; Di Girolamo et al., 2010; Liang et al., 2009; Zhang & Platnick, 2011; Zhang et al., 2012). For this pixel $H_{\sigma,V}$ is 0.02, while for the SWIR band reflectance the respective inhomogeneity index is $H_{\sigma,S} = 0.03$. The white plus sign, indicating the position of mean reflectances \bar{R}_V and \bar{R}_S , is centered right in the middle of the 30-m subpixel values.

Following the definitions of Cahalan and Joseph (1989), Marshak et al. (2006), and Z16, the PPHB for cloud optical thickness ($\Delta\tau$) and effective droplet radius (Δr_{eff}) can be expressed as the difference between the cloud property retrievals based on the mean subpixel reflectances and the mean values of the actual subpixel retrievals:

$$\begin{aligned} \Delta\tau &= \tau\left(\bar{R}_V, \bar{R}_S\right) - \tau\left(R_V, R_S\right) \\ \Delta r_{\text{eff}} &= r_{\text{eff}}\left(\bar{R}_V, \bar{R}_S\right) - r_{\text{eff}}\left(R_V, R_S\right). \end{aligned} \quad (2)$$

Using equation (2) to assess the PPHB of the homogeneous pixel shown in Figure 1 yields low PPHB values of $\Delta\tau = -0.07$ and $\Delta r_{\text{eff}} = -0.01 \mu\text{m}$. Conversely, the red dots illustrate a 960-m pixel containing a rather inhomogeneous cloud, where a large variability in subpixel R_V and R_S at 30 m exists. For this example pixel $H_{\sigma,V} = 0.41$ and $H_{\sigma,S} = 0.25$. As a result, the observed PPHB values of $\Delta\tau = -3.59$ and $\Delta r_{\text{eff}} = 1.40 \mu\text{m}$ are much larger.

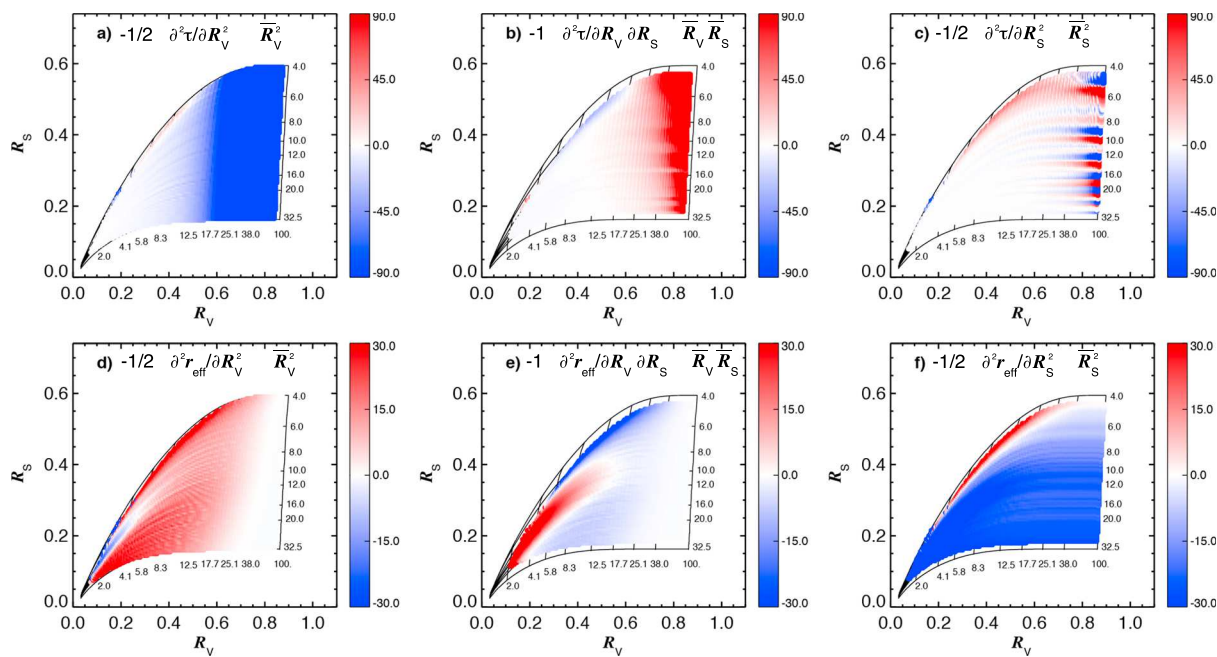


Figure 2. Example lookup table from Advanced Spaceborne Thermal Emission and Reflection Radiometer band 3N reflectances R_V in the visible to near-infrared spectral wavelength range and band 5 reflectances R_S in the shortwave-infrared spectral wavelength range. Colors illustrate the values of the six individual terms of the matrix of second derivatives in equation (3), namely, (a) $-\frac{1}{2} \frac{\partial^2 \tau(\bar{R}_V, \bar{R}_S)}{\partial^2 R_V} \bar{R}_V^{-2}$, (b) $-\frac{\partial^2 \tau(\bar{R}_V, \bar{R}_S)}{\partial R_V \partial R_S} \bar{R}_V \bar{R}_S$, (c) $-\frac{1}{2} \frac{\partial^2 \tau(\bar{R}_V, \bar{R}_S)}{\partial^2 R_S} \bar{R}_S^{-2}$, (d) $-\frac{1}{2} \frac{\partial^2 r_{\text{eff}}(\bar{R}_V, \bar{R}_S)}{\partial^2 R_V} \bar{R}_V^{-2}$, (e) $-\frac{\partial^2 r_{\text{eff}}(\bar{R}_V, \bar{R}_S)}{\partial R_V \partial R_S} \bar{R}_V \bar{R}_S$, and (f) $-\frac{1}{2} \frac{\partial^2 r_{\text{eff}}(\bar{R}_V, \bar{R}_S)}{\partial^2 R_S} \bar{R}_S^{-2}$.

At this point it should be noted that the variability in the reflectances R_V and R_S , as well as the variability in the respective subpixel τ and r_{eff} retrievals, may be caused by 3-D radiative effects instead of actual changes in the underlying cloud structure (Davis & Marshak, 2010; Marshak et al., 2006). These effects, caused by the independent treatment of cloudy columns in the IPA approach, cannot be explained by 1-D plane-parallel radiative transfer. The PPHB just describes the statistical difference between subpixel and pixel-level retrievals due to an observed reflectance variability in combination with the nonlinearity of the LUT. However, the high-resolution subpixel results might be additionally biased due to 3-D radiative effects (e.g., cloud shadows and illuminated cloud sides).

3.2. Mathematical Framework for PPHB Prediction

The two examples in Figure 1 illustrate that the combined subpixel variability in R_V and R_S determines the PPHB biases $\Delta\tau$ and Δr_{eff} . The discussion in Z16 shows that the sign and magnitude of $\Delta\tau$ and Δr_{eff} can be investigated by expanding the respective cloud optical and microphysical properties into two-dimensional Taylor series of R_V and R_S , which in matrix form is as follows:

$$\begin{pmatrix} \Delta\tau \\ \Delta r_{\text{eff}} \end{pmatrix} = \begin{pmatrix} \tau(\bar{R}_V, \bar{R}_S) - \bar{\tau}(R_V, R_S) \\ r_{\text{eff}}(\bar{R}_V, \bar{R}_S) - \bar{r}_{\text{eff}}(R_V, R_S) \end{pmatrix} = \begin{pmatrix} -\frac{1}{2} \frac{\partial^2 \tau(\bar{R}_V, \bar{R}_S)}{\partial^2 R_V} \bar{R}_V^{-2} & -\frac{1}{2} \frac{\partial^2 \tau(\bar{R}_V, \bar{R}_S)}{\partial R_V \partial R_S} \bar{R}_V \bar{R}_S & -\frac{1}{2} \frac{\partial^2 \tau(\bar{R}_V, \bar{R}_S)}{\partial^2 R_S} \bar{R}_S^{-2} \\ -\frac{1}{2} \frac{\partial^2 r_{\text{eff}}(\bar{R}_V, \bar{R}_S)}{\partial^2 R_V} \bar{R}_V^{-2} & -\frac{1}{2} \frac{\partial^2 r_{\text{eff}}(\bar{R}_V, \bar{R}_S)}{\partial R_V \partial R_S} \bar{R}_V \bar{R}_S & -\frac{1}{2} \frac{\partial^2 r_{\text{eff}}(\bar{R}_V, \bar{R}_S)}{\partial^2 R_S} \bar{R}_S^{-2} \end{pmatrix} \cdot \begin{pmatrix} \text{cov}(R_V, R_S) \\ \sigma_S^2 \end{pmatrix} = \begin{pmatrix} -\frac{1}{2} \frac{\partial^2 \tau(\bar{R}_V, \bar{R}_S)}{\partial^2 R_V} \bar{R}_V^{-2} & -\frac{1}{2} \frac{\partial^2 \tau(\bar{R}_V, \bar{R}_S)}{\partial R_V \partial R_S} \bar{R}_V \bar{R}_S & -\frac{1}{2} \frac{\partial^2 \tau(\bar{R}_V, \bar{R}_S)}{\partial^2 R_S} \bar{R}_S^{-2} \\ -\frac{1}{2} \frac{\partial^2 r_{\text{eff}}(\bar{R}_V, \bar{R}_S)}{\partial^2 R_V} \bar{R}_V^{-2} & -\frac{1}{2} \frac{\partial^2 r_{\text{eff}}(\bar{R}_V, \bar{R}_S)}{\partial R_V \partial R_S} \bar{R}_V \bar{R}_S & -\frac{1}{2} \frac{\partial^2 r_{\text{eff}}(\bar{R}_V, \bar{R}_S)}{\partial^2 R_S} \bar{R}_S^{-2} \end{pmatrix} \cdot \begin{pmatrix} H_{\sigma_V}^2 \\ H_{\text{cov}} \\ H_{\sigma_S}^2 \end{pmatrix}. \quad (3)$$

Here σ_V^2 and σ_S^2 are the spatial variances, while $\text{cov}(R_V, R_S)$ is the spatial covariance of the reflectances R_V and R_S . Equation (3) consists of two parts: a vector $[\sigma_V^2, \text{cov}(R_V, R_S), \sigma_S^2]^T$, which describes the sampled subpixel variability of R_V and R_S , and a matrix containing the second-order derivatives of the LUT. The former can be

easily calculated from high-resolution measurements, while the latter can be derived from numerical differentiation within the applied LUT. Note that by multiplying each matrix element with the respective mean reflectances the terms σ_v^2 , $\text{cov}(R_v, R_s)$, and σ_s^2 can be easily substituted with the commonly used inhomogeneity indices $H_{\sigma_v}^2 = \sigma_v^2 / \overline{R_v}^2$ and $H_{\sigma_s}^2 = \sigma_s^2 / \overline{R_s}^2$ following equation (1), as well as the relative covariance term $H_{\text{cov}} = \text{cov}(R_v, R_s) / \overline{R_v} \overline{R_s}$.

Figures 2a–2f show an example of each of the six matrix elements. The LUT is derived for the respective solar and viewing geometry for ASTER observations on 8 March 2005 at 19:08:35 (case C7 in Werner et al., 2016). The two PPHB contributions discussed in Marshak et al. (2006), illustrated in Figure 2a for $\Delta\tau$ and 2f for Δr_{eff} , are almost universally negative, indicating that the retrievals based on aggregated reflectances are smaller than the actual subpixel mean values. However, the contributions from the respective secondary bands (R_s in the τ retrieval and R_v in the r_{eff} retrieval) show a more complex behavior and can be strongly positive, as shown in Figures 2c and 2d. Similar observations hold true for contributions from the covariance term, shown in Figures 2b and 2e. This means that the sampled subpixel reflectance variability is not the only important variable determining the PPHB. The retrieval sensitivity and the respective position of the measurements in the LUT are equally important. Generally, the sign of $\Delta\tau$ is dominated by the first matrix element and mostly negative (except for very large τ). In contrast, the sign and magnitude of Δr_{eff} are influenced by all three matrix elements and vary strongly, especially for small τ . Note that the apparent striping pattern in some of the matrix elements (e.g., in Figure 2c) is caused by artifacts in the applied numerical derivation algorithm. For this work, the numerical derivatives are calculated with a central differences scheme and a reflectance interval of 0.02. An increase in LUT resolution, a decrease of the reflectance interval and the application of different numerical derivation schemes with lower truncation errors can mitigate these artifacts, while increasing the computational costs of the derivation algorithm.

3.3. PPHB for PCL Pixels

Two significant factors make it difficult to calculate and predict the PPHB for PCL pixels. The first issue arises from the definition of $\Delta\tau$ and Δr_{eff} in equation (2), where the sign and magnitude of, for example, $\Delta\tau$, are determined by a pixel-level ($\tau(\overline{R_v}, \overline{R_s})$) and a subpixel term ($\tau(R_v, R_s)$). For PCL pixels the two terms are composed of different subpixel populations. Whereas the pixel-level term is retrieved from the mean of all subpixel reflectances, the subpixel term is only defined for the cloudy part of the pixel (i.e., a clear subpixel has no defined τ and r_{eff} and thus is not represented in the mean value). While it is conceivable that a value of $\tau = 0$ could be assigned to a clear subpixel, similar considerations for the effective droplet radius are not valid (i.e., a value of $r_{\text{eff}} = 0 \mu\text{m}$ is unphysical).

Moreover, the general characteristics of the Taylor series expansion might prevent a reliable estimate of the PPHB following equation (3) if a pixel is PCL. The Taylor series is a series expansion of a real function about a point. Most well-behaved functions can be reliably approximated by a finite number of terms, and the remaining error is comparatively small. However, very complex functions might require a series expansion up to a large order (\mathcal{O}) to reliably approximate the original function. Even then, the remaining error might be significant. For PCL pixels, the cloudy subpixels exhibit a reflectance distribution similar to the ones shown in Figure 1, where R_v and R_s are largely determined by the underlying cloud characteristics. The reflectances from the clear subpixels, meanwhile, are likely outside the LUT and clustered in the lower left corner (i.e., very low R_v and R_s). Representing such a distribution with a second-order Taylor series ($\mathcal{O} = 2$) likely yields unreliable results with a large remaining error.

In order to successfully apply the mathematical framework presented in section 3.2 to PCL pixels, retrievals based on only cloudy R_v and R_s are required. Studies by Han et al. (1994) and Coakley et al. (2005) discuss the impact of surface contamination on the retrieval products of PCL pixels and propose methods to estimate the cloudy part reflectances and cloud variables. High-resolution ASTER data provide the opportunity to evaluate and expand on these approaches in future studies and will allow to further test the PPHB correction for PCL pixels.

4. Correction of Observed PPHB

In this section ASTER reflectance observations at 30-m horizontal resolution are used to predict the PPHB based on equation (3). The predicted PPHB results are compared to the actually observed biases, first for a case study (section 4.1) and subsequently in a statistical analysis for 48 MBL scenes (section 4.2).

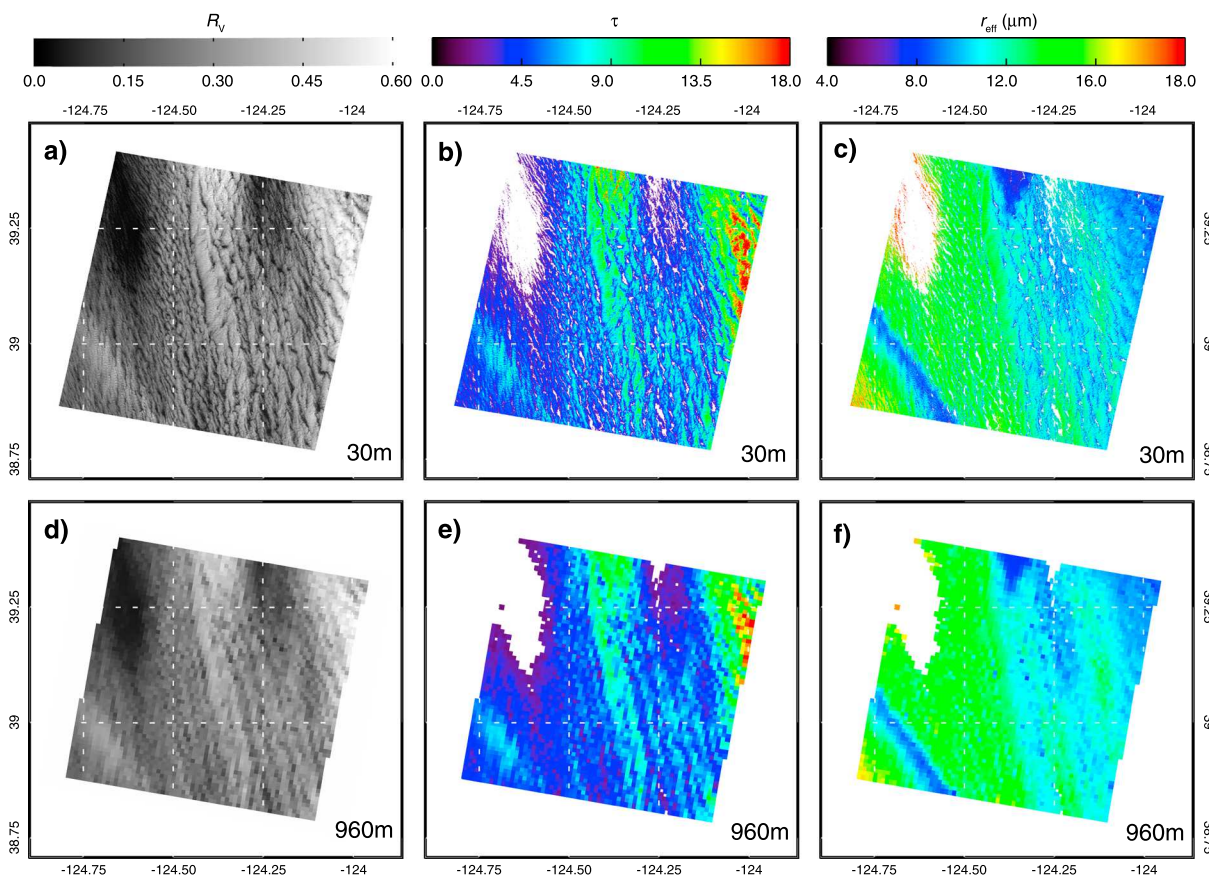


Figure 3. (a) Single-band grayscale image of band 3N reflectances sampled by Advanced Spaceborne Thermal Emission and Reflection Radiometer off the coast of California on 8 March 2005 at 19:08:35. The horizontal resolution is 30 m. (b) Same as (a) but for the retrieved cloud optical thickness τ . (c) Same as (a) but for the effective droplet radius r_{eff} . (d–f) Same as (a)–(c) but for a horizontal resolution of 960 m.

4.1. Case Study

Figure 3a shows a grayscale image of R_v at 30-m horizontal resolution. Data were sampled on 8 March 2005 at 19:08:35 UTC. This example depicts a rather complex and inhomogeneous MBL cloud scene with a number of cloud holes (around 124.60°W, 39.25°N and 124.25°W, 39.25°N), larger areas of thin clouds and three areas of increased cloud reflectance (located in the southwest, middle, and northeast of the granule). Retrieved τ and r_{eff} are shown in Figures 3b and 3c. Most of the scene exhibits retrievals ranging from $\tau = 5$ to 10 and $r_{\text{eff}} = 12$ to 16 μm , whereas the thick cloudy regions are characterized by $\tau > 11$ and $r_{\text{eff}} = 8$ –10 μm . Some extreme values of $\tau > 17$ and $r_{\text{eff}} < 8 \mu\text{m}$ (around the thick clouds) and $\tau < 2$ and $r_{\text{eff}} > 17 \mu\text{m}$ (around the cloud edges) can be observed. Decreasing the spatial resolution to 960 m (i.e., a MODIS-like horizontal resolution) yields a much smoother cloud field, as illustrated in Figures 3d–3f. Here the lowest and highest retrieval observations are much less frequent, which is especially obvious for the large optical thickness values shown in Figure 3b.

Maps of observed $\Delta\tau$ and Δr_{eff} , based on equation (2) and shown in blue and red colors (depending on sign and magnitude), are provided in Figures 4a and 4d, respectively. Here the mean values $\tau(R_v, R_s)$ and $r_{\text{eff}}(R_v, R_s)$ are calculated from the high-resolution retrievals based on 30-m ASTER observations, while $\tau(\bar{R}_v, \bar{R}_s)$ and $r_{\text{eff}}(\bar{R}_v, \bar{R}_s)$ are the retrievals based on aggregated reflectances at 960 m. Following the discussion in section 3.3, the PPHB is only calculated for pixels with a subpixel cloud cover of $C_{\text{sub}} = 1.0$. Pixels with $C_{\text{sub}} < 1.0$ are shown in gray colors and are not included in the analysis. For this MBL scene $\Delta\tau$ and Δr_{eff} are almost exclusively negative and positive, respectively, with $-0.55 < \Delta\tau < -0.01$ and $-0.03 \mu\text{m} < \Delta r_{\text{eff}} < 0.92 \mu\text{m}$. The largest $\Delta\tau$ (in magnitude) are obtained for pixels containing thick clouds (see Figure 3 for comparison), while the thin cloud regions exhibit the largest Δr_{eff} . The predicted PPHB results, derived from equation (3) and the matrix elements illustrated in Figure 2, are shown in Figure 4b for $\Delta\tau$ and Figure 4e for Δr_{eff} . It is obvious that both the sign and magnitude of the predicted PPHB results agree well

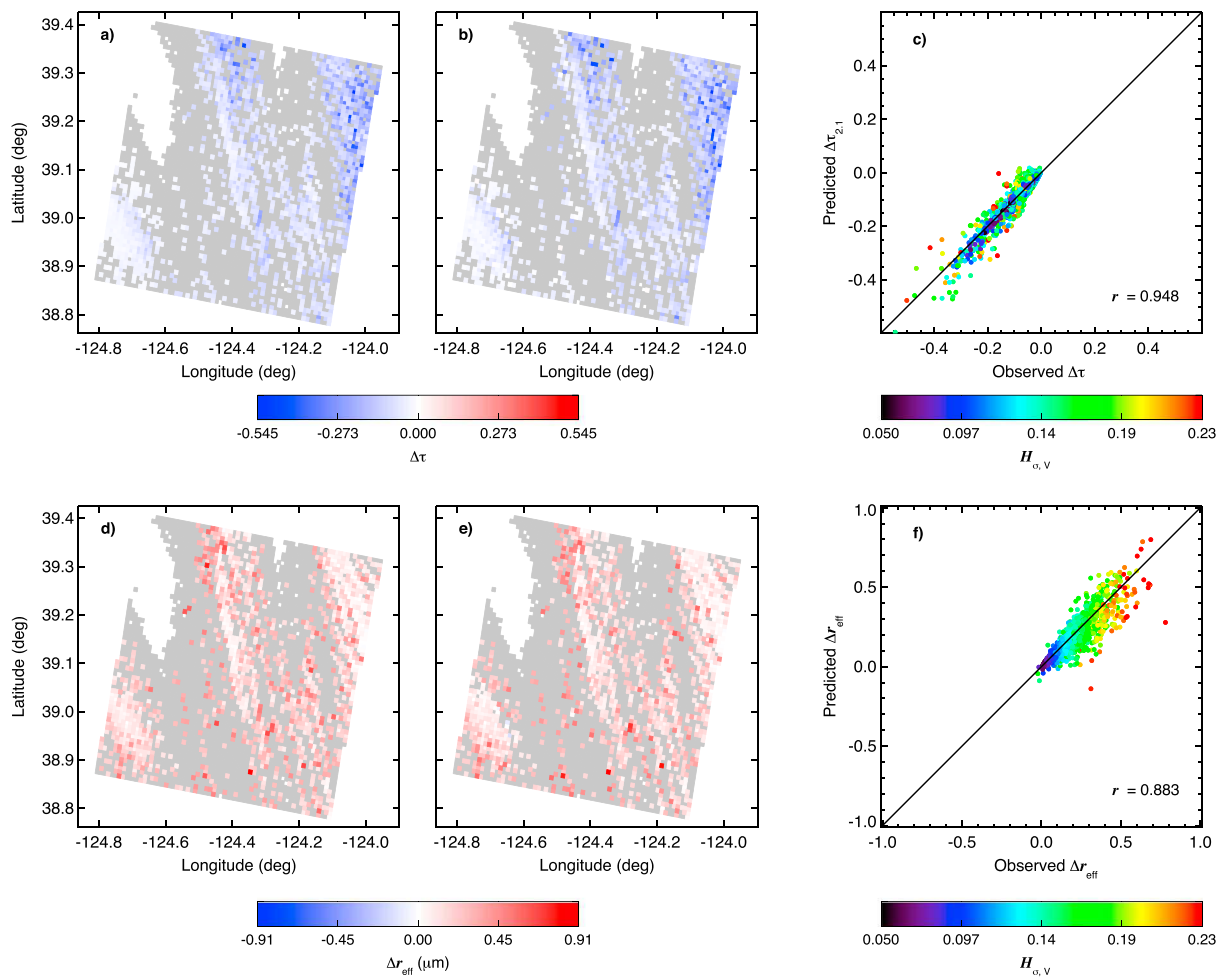


Figure 4. (a) Observed plane-parallel homogeneous bias (PPHB), derived from subpixel data with a horizontal resolution of 30-m and pixel-level data with a horizontal resolution of 960 m, for the cloud optical thickness τ for the Advanced Spaceborne Thermal Emission and Reflection Radiometer cloud scene sampled off the coast of California on 8 March 2005 at 19:08:35. Colors indicated the magnitude and sign of the PPHB; gray colors indicate pixels with a subpixel cloud cover $C_{\text{sub}} < 1$. (b) Same as (a) but for the predicted PPHB based on equation (3). (c) Scatter plot of observed versus predicted PPHB for τ for all pixels with $C_{\text{sub}} = 1$. Colors indicate the respective pixel value of the inhomogeneity index of Advanced Spaceborne Thermal Emission and Reflection Radiometer 3B reflectances $H_{\sigma,V}$. (d–f) Same as (a)–(c) but for the effective droplet radius Δr_{eff} .

with the actually observed values shown in Figures 4a and 4d. A pixel-level comparison between the predicted and observed PPHB is shown in Figures 4c and 4f for $\Delta\tau$ and Δr_{eff} , respectively. Colors indicate the value of the subpixel inhomogeneity index $H_{\sigma,V}$. The objectively good agreement between predicted and observed PPHB seen in the maps in Figure 4 is confirmed, with data points close to the 1:1 line and high values of Pearson's product-moment correlation coefficient of $r \geq 0.88$. For $\Delta\tau$ there seems to be no dependence on $H_{\sigma,V}$; however, there is an increase of Δr_{eff} with an increase in $H_{\sigma,V}$. Overall, the prediction works better for $\Delta\tau$ than for Δr_{eff} , which can be attributed to the more complex distribution of the matrix elements shown in Figures 2d–2f. All three matrix elements have a strong contribution to the total Δr_{eff} , while small changes in R_V or R_S can switch the sign of Δr_{eff} from positive to negative, especially for small optical thicknesses (e.g., illustrated by the thin negative stripe in Figure 2d). Such significant changes in sign and magnitude do not exist in the three matrix elements for $\Delta\tau$, which makes the predicted Δr_{eff} more sensitive to uncertainties in the sampled R_V and R_S . For small reflectances (i.e., thin clouds) there is also an overall decrease in retrieval sensitivity for r_{eff} due to the convergence of the respective LUT isolines (Cho et al., 2015; Werner et al., 2013, 2016). As a result, the increased retrieval uncertainty for $r_{\text{eff}}(\overline{R_V}, \overline{R_S})$ and $\overline{r_{\text{eff}}}(R_V, R_S)$ impacts not only the calculation of the numerical derivatives but also the actually observed Δr_{eff} .

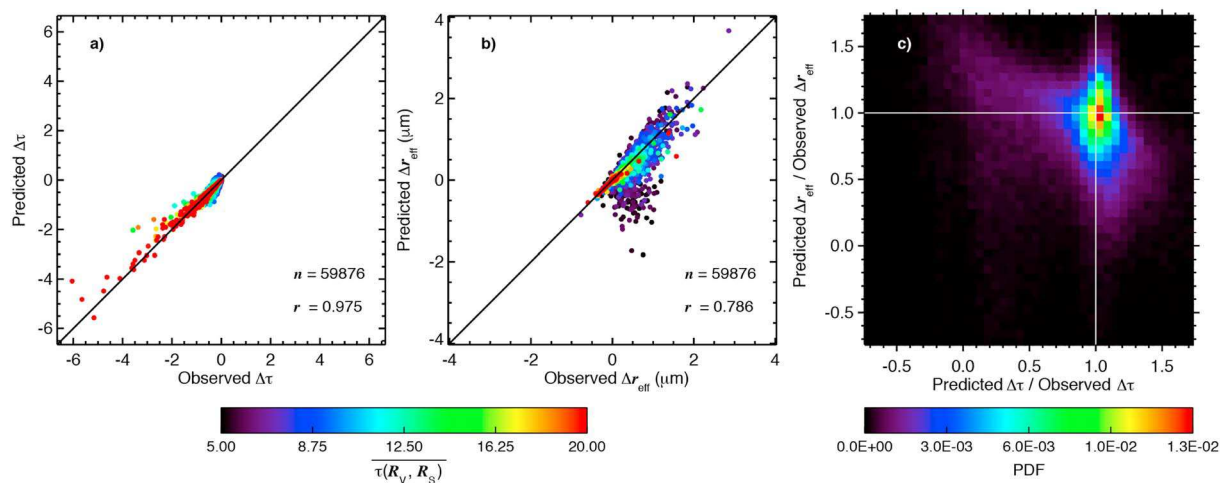


Figure 5. (a) Scatter plot of observed versus predicted plane-parallel homogeneous bias (PPHB) for the cloud optical thickness τ , derived from subpixel data with a horizontal resolution of 30 m and pixel-level data with a horizontal resolution of 960 m. Data are from 48 marine boundary layer scenes sampled off the coast of California, amounting to $n = 59,876$ pixels with a subpixel cloud cover $C_{\text{sub}} = 1$. Colors indicate the respective pixel value of $\tau(R_V, R_S)$. (b) Same as (a) but for the effective droplet radius r_{eff} . (c) Joint probability density (PDF) function of the ratio of predicted to observed PPHB for τ and the ratio of predicted to observed PPHB for r_{eff} .

4.2. Statistics

The results in Figure 4 reveal a good agreement between observed PPHB and the predicted values based on the framework presented in section 3. To confirm these findings and test the viability of the framework for a wide array of inhomogeneous cloud cases, similar analysis is performed for the 48 MBL scenes introduced in Werner et al. (2016). As for the case study, only pixels with $C_{\text{sub}} = 1.0$ are included, which yields a data set of $n = 59,876$ pixels. The pixel-level comparison between observed and predicted $\Delta\tau$ and Δr_{eff} is shown in Figures 5a and 5b, where colors indicate the mean subpixel cloud optical thickness $\tau(R_V, R_S)$.

The observed PPHB for all scenes, as derived from ASTER retrievals using equation (2), is in the range of $-6.05 < \Delta\tau < 0.05$ and $-0.78 \mu\text{m} < \Delta r_{\text{eff}} < 2.86 \mu\text{m}$, respectively. Similar to the case study in Figure 4, there is a good agreement between observed and predicted PPHB with high correlation coefficients of $r = 0.98$ ($\Delta\tau$) and $r = 0.79$ (Δr_{eff}). The prediction based on equation (3) seems to be particularly good for thicker clouds with $\tau(R_V, R_S) > 5$. Similar to the case study, the correlation between observed and predicted PPHB gets lower for clouds with a low optical thickness $\tau(R_V, R_S) < 5$, which is especially obvious for Δr_{eff} . Excluding these thin clouds from the analysis increases the correlation coefficient between observed and predicted Δr_{eff} from $r = 0.79$ to $r = 0.87$. A clear relationship between cloud optical thickness and PPHB exists, as the highest Δr_{eff} exist for pixels with low $\tau(R_V, R_S)$. For $\Delta\tau$ the behavior is not as pronounced, but generally, there is an increase in the absolute values of the PPHB with an increase in $\tau(R_V, R_S)$. Figure 5c shows the joint probability density function (PDF) of the ratios of predicted to observed $\Delta\tau$ and Δr_{eff} . Most observations show ratios of unity, confirming the good agreement between predicted and observed PPHB. About 70% of all data points are characterized by a ratio of observed to predicted $\Delta\tau$ in the range of 0.8–1.2. The spread for the ratio of observed to predicted Δr_{eff} is larger, with 80% of all data points covering the range 0.5–1.5.

The results presented in Figures 4 and 5 show that knowledge about the subpixel reflectance variability, in combination with equation (3), can be applied to successfully predict $\Delta\tau$ and Δr_{eff} for the 48 MBL scenes in this study. This also means, that the difference between the actually obtained mean values of the subpixel retrievals $\tau(R_V, R_S)$ and $\bar{r}_{\text{eff}}(R_V, R_S)$ at a horizontal resolution of 30 m and the pixel-level retrievals based on aggregated reflectances at 960 m, can be mitigated by correcting $\tau(R_V, R_S)$ and $r_{\text{eff}}(R_V, R_S)$ with the predicted $\Delta\tau$ and Δr_{eff} . Figure 6a shows the joint PDF of the ratio of observed $\tau(R_V, R_S)$ to $\bar{r}_{\text{eff}}(R_V, R_S)$ (i.e., the ratio of retrievals based on aggregated reflectances to the mean subpixel retrievals) and $\tau(R_V, R_S)$. A ratio of 1 indicates that there is no PPHB, while ratios smaller (larger) than 1 indicate a negative (positive) PPHB. The primarily negative $\Delta\tau$, illustrated in Figure 5a, leads to an obvious negative bias in the τ retrievals based on aggregated reflectances, with underestimations of up to 7% for thin clouds. With increasing $\tau(R_V, R_S)$

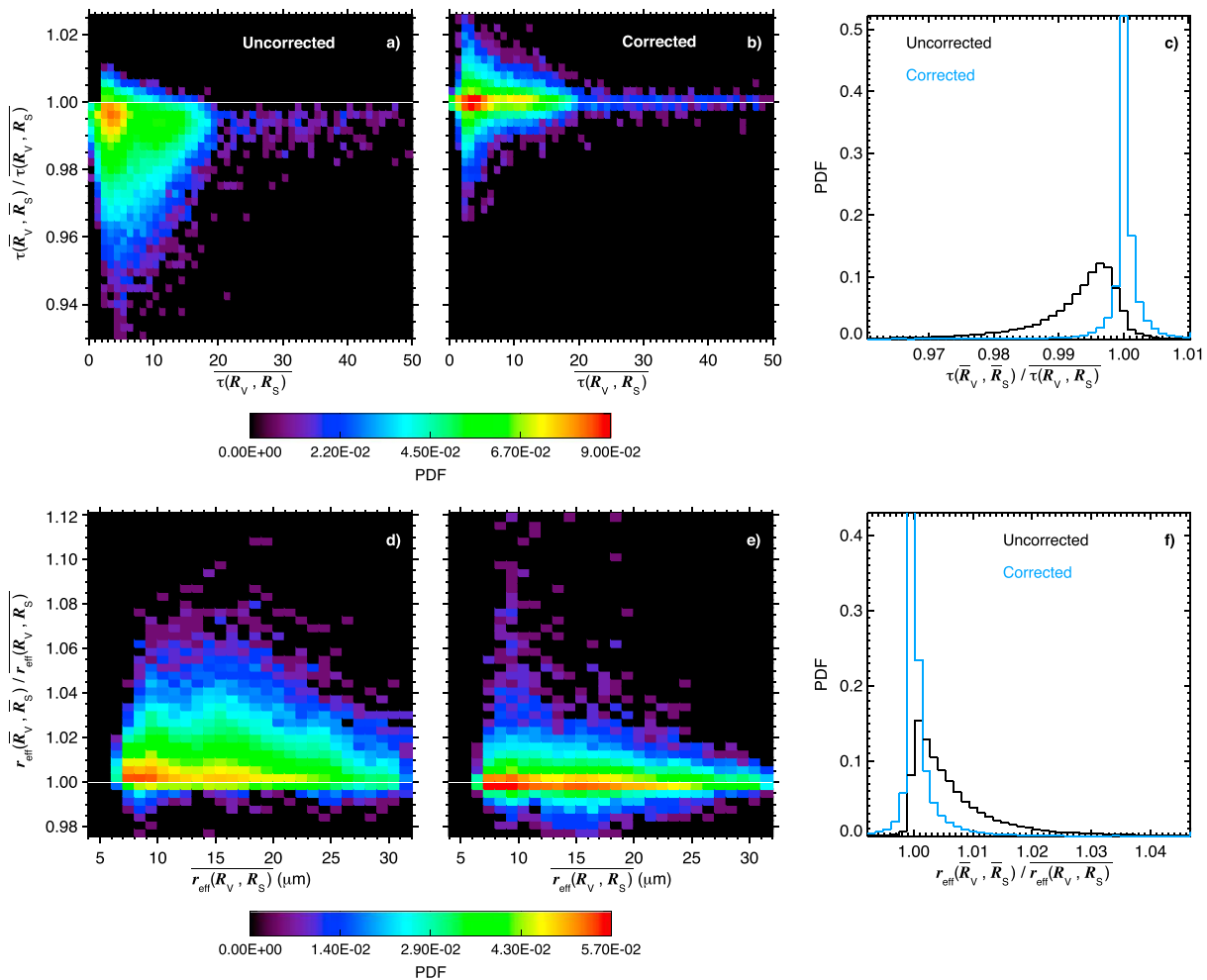


Figure 6. (a) Joint probability density function (PDF) of the ratio of observed $\tau(\bar{R}_V, \bar{R}_S)$ to $\tau(R_V, R_S)$ and $\tau(\bar{R}_V, \bar{R}_S)$. Values have been derived from subpixel data with a horizontal resolution of 30 m and pixel-level data with a horizontal resolution of 960 m. (b) Same as (a) but for the observed $\tau(\bar{R}_V, \bar{R}_S)$, which has been corrected by the predicted $\Delta\tau$, based on equation (3). (c) PDFs of the ratio of observed $\tau(\bar{R}_V, \bar{R}_S)$ to $\tau(R_V, R_S)$ (black) and the ratio of observed $\tau(\bar{R}_V, \bar{R}_S)$, which has been corrected by the predicted $\Delta\tau$, to $\tau(R_V, R_S)$ (blue). (d–f) Same as (a)–(c) but for the effective droplet radius r_{eff} .

these underestimations converge to a value of about 2%. Figure 6b shows the results of a correction of the retrieved $\tau(\bar{R}_V, \bar{R}_S)$ with the predicted PPHB values based on equation (3). The overall negative bias illustrated in Figure 6a is gone after the correction and most observations (red colors) show a ratio of 1, indicating that the mean of the subpixel retrievals and $\tau(\bar{R}_V, \bar{R}_S)$ are in close agreement. The maximum $\Delta\tau$ for thin clouds is reduced to about $\pm 3\%$. PDFs of the ratio of $\tau(\bar{R}_V, \bar{R}_S)$ to $\tau(R_V, R_S)$ are shown in Figure 5c for both the uncorrected (black) and corrected (blue) data set. It is clear that by correcting τ retrievals based on aggregated reflectances with the predicted $\Delta\tau$ the mean of the subpixel retrievals can be successfully reproduced. A ratio close to 1 (i.e., no PPHB) is obtained for over 50% of all pixels, while the overall negative bias for $\tau(\bar{R}_V, \bar{R}_S)$ is removed. Without a PPHB correction the normalized root-mean-square deviation between pixel-level and subpixel retrievals (nRMSD, defined as the RMSD normalized by the mean of the subpixel results) is 1.4%, while the 1st and 99th percentiles of the ratio of $\tau(\bar{R}_V, \bar{R}_S)$ to $\tau(R_V, R_S)$ are 0.960 and 1.003, respectively. After a correction of the pixel-level retrievals with the predicted $\Delta\tau$ the nRMSD = 0.25% and the 1st and 99th percentiles are 0.991 and 1.010.

Similar analysis for Δr_{eff} is presented in Figures 6d–6f. A positive PPHB of up to 12% exists and overall strong overestimations in the range of 5% exist over the whole observable $\bar{r}_{\text{eff}}(R_V, R_S)$ range. The correction of the PPHB with predicted Δr_{eff} again yields considerable improvements, as most observations (red colors) exhibit

a ratio of $r_{\text{eff}}(\overline{R_V}, \overline{R_S})$ to $\overline{r_{\text{eff}}}(R_V, R_S)$ close to 1. Most pixels are characterized by a good agreement between subpixel means and pixel-level retrievals in the range of $\pm 2\%$. An area of strong overestimations of up to 12% remains (around $\overline{r_{\text{eff}}}(R_V, R_S) = 8 - 10 \mu\text{m}$), which is associated with low $\overline{\tau}(R_V, R_S) < 5$. Excluding pixels with $\overline{\tau}(R_V, R_S) < 5$ from the analysis yields a joint PDF were considerably less of these pixel-level overestimations remain. Figure 6d shows PDFs of the ratio of pixel-level retrievals (based on aggregated reflectances) to $\overline{r_{\text{eff}}}(R_V, R_S)$, again for the data set with and without the applied corrections with predicted Δr_{eff} . Similar to the cloud optical thickness results, over 40% of pixels show a ratio of 1 and the 1st and 99th percentiles change from 0.998 and 1.047 to 0.992 and 1.025, respectively. Again, the nRMSD is significantly reduced from 1.4% to 0.87%. This indicates that the correction based on equation (3) yields an improved agreement between $r_{\text{eff}}(\overline{R_V}, \overline{R_S})$ and $\overline{r_{\text{eff}}}(R_V, R_S)$.

The liquid water path (*LWP*), while not an input parameter for the radiative transfer simulations to generate the LUT for the retrievals, is the primary parameter that determines cloud shortwave radiative forcing and is an essential variable in the evaluation of climate models (Jiang et al., 2012). It can be derived as the product of retrieved τ and r_{eff} (Miller et al., 2016):

$$LWP = \Gamma \cdot \rho_l \cdot \tau \cdot r_{\text{eff}}, \quad (4)$$

where ρ_l is the density of liquid water and Γ is a coefficient linked to assumptions about the vertical cloud profile (here $\Gamma = 2/3$, assuming vertically homogeneous clouds). Similar to $\Delta\tau$ and Δr_{eff} , ΔLWP was derived for all pixels and compared to the predicted values from the mathematical framework presented in section 3.2. Since the pixel-level retrievals $\tau(\overline{R_V}, \overline{R_S})$ and $r_{\text{eff}}(\overline{R_V}, \overline{R_S})$ are usually biased low and high, respectively, and both biases are comparable in magnitude, ΔLWP is rather small. The 1st and 99th percentiles of the ratio of uncorrected pixel-level to mean subpixel *LWP* for all analyzed pixels are 0.974 and 1.037, while about 18% of data exhibit a ratio of 1 (i.e., the distribution is centered around 1). The correction of the pixel-level results with predicted ΔLWP slightly reduces these maximum deviations to 0.979 and 1.036, respectively, and about 29% of pixels show a ratio of 1. Moreover, the nRMSD changes from 1.79% to 0.93%. Thus, the correction of pixel-level *LWP* with ΔLWP yields results that are closer to the mean subpixel observations. The correlation between observed and predicted ΔLWP is $r = 0.86$, which is comparable to the correlation for Δr_{eff} .

The statistical analysis from over $n = 59,876$ pixels, sampled over 48 MBL cloud scenes, illustrates that the mathematical framework presented in section 3 can be successfully applied to predict and subsequently mitigate the PPHB. As mentioned in section 3.1, the correction of $\tau(\overline{R_V}, \overline{R_S})$ and $r_{\text{eff}}(\overline{R_V}, \overline{R_S})$ (i.e., the lower-resolution, pixel-level retrievals) with the predicted $\Delta\tau$ and Δr_{eff} values yields retrievals that are in close agreement with the mean subpixel results. However, $\tau(R_V, R_S)$ and $\overline{r_{\text{eff}}}(R_V, R_S)$ might be biased due to 3-D radiative effects and therefore may not represent the true, high-resolution cloud properties.

5. Practical Implementation

The analysis in section 4 demonstrates that samples of high-resolution VNIR and SWIR reflectances on the subpixel scale can be applied to explain and correct the observed PPHB of the pixel-level retrievals $\tau(\overline{R_V}, \overline{R_S})$ and $r_{\text{eff}}(\overline{R_V}, \overline{R_S})$. However, most satellite missions only provide limited subpixel reflectance information, affecting the determination of the vector of subpixel reflectance variability in equation (3). While retrievals of τ and r_{eff} by MODIS are based on aggregated reflectances at a similar horizontal resolution of 1,000 m, subpixel reflectance data in the VNIR and SWIR are sampled at 250- and 500-m horizontal resolutions, respectively. Similarly, VIIRS provides 4×4 subpixel VNIR and SWIR reflectances at 375-m horizontal resolution, while the cloud property retrievals are performed for larger pixels with a horizontal resolution of 750 m. Finally, the SEVIRI includes just a single high-resolution visible band (centered around $\lambda = 0.75 \mu\text{m}$) with a horizontal resolution of 1,000 m that yields subpixel reflectances within each $(3,000 \times 3,000)-m pixel. It is therefore essential to study the implications of different horizontal resolutions, as well as limitations in the availability of high-resolution bands, on the viability of the PPHB prediction. The analysis in section 5.1 provides information about the behavior of the elements of the subpixel variability vector in equation (3) with changes in pixel-level and subpixel horizontal resolution, while section 5.2 presents statistics of $\Delta\tau$ and Δr_{eff} for different combinations of subpixel and pixel-level scales. Section 5.3 discusses the result of a PPHB correction with only high-resolution VNIR band reflectances.$

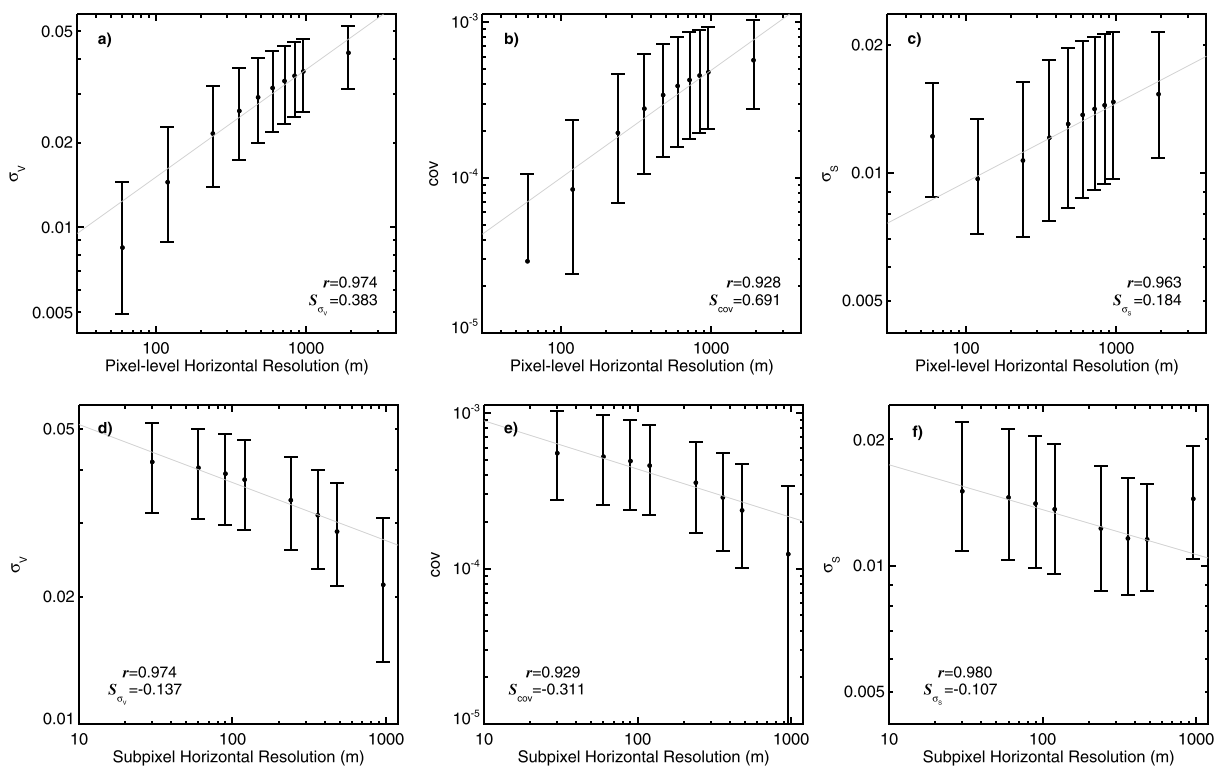


Figure 7. (a) Median (dots) and interquartile range of the standard deviation of 30-m visible to near-infrared spectral wavelength range (VNIR) reflectances (σ_V) as a function of pixel-level horizontal resolution. Data are from 48 marine boundary layer scenes sampled off the coast of California. The gray diagonal line represents a linear regression through the data in log-log space (the first data point at 60-m horizontal resolution is omitted in the calculation of the regression). The correlation coefficient (r) between data and regression, as well as the slope (i.e., relative susceptibility S_{σ_V}), are given. (b) Same as (a) but for the covariance of 30-m VNIR and shortwave-infrared spectral wavelength range reflectances ($\text{cov}(R_V, R_S)$). (c) Same as (a) but for the standard deviation of 30-m shortwave-infrared spectral wavelength range reflectances (σ_S). (d) Derived σ_V from subpixel VNIR reflectances at different horizontal resolutions. The pixel-level scale is 1,920 m. The gray diagonal line represents a linear regression through the data in log-log space (the last data point at 960-m horizontal resolution is omitted in the calculation of the regression). (e) Same as (d) but for $\text{cov}(R_V, R_S)$. (f) Same as (d) but for σ_S .

5.1. Scale Dependence of Subpixel Variability

The results presented in sections 4.1 and 4.2 are based on subpixel ASTER observations with a horizontal resolution of 30 m and pixel-level data with a horizontal resolution of 960 m. If η is the number of available subpixels, there are $\eta = 32 \cdot 32 = 1,024$ pixels with a horizontal resolution of 30 m within each (960×960) -m pixel. For a fixed pixel-level horizontal resolution the matrix of second-order derivatives in equation (3) is not dependent on η , while the subpixel variability vector $[\sigma_V^2, \text{cov}(R_V, R_S), \sigma_S^2]^T$ might change significantly with a change in η . Conversely, for a fixed subpixel horizontal resolution the matrix of second-order derivatives (due to a change in \bar{R}_V and \bar{R}_S), as well as the subpixel variability vector, are affected by a change in pixel-level scale.

Figure 7a shows the behavior of σ_V at 30 m (i.e., the first element of the subpixel variability vector) for pixel-level resolutions between 60 m ($\eta = 2 \cdot 2 = 4$) and 1,920 m ($\eta = 64 \cdot 64 = 4,096$), respectively. Dots show the median of all overcast pixels for each pixel-level scale, while vertical bars indicate the interquartile range (75th–25th percentile of all pixels). Because the increase of σ_V with increasing pixel-level scale seems to follow a power law (as reported by Cahalan, Ridgway, Wiscombe, & Bell, 1994, for fractal clouds), the relationship between the two variables is illustrated in a log-log diagram, where the logarithmic behavior becomes almost linear. Similar relationships between $\text{cov}(R_V, R_S)$ and σ_S (i.e., the second and third elements of the subpixel variability vector) and pixel-level scale are evident in Figures 7b and 7c. However, the power law behavior seems to break down for $\eta = 4$ (i.e., 30-m observations within a 60-m pixel) and the median values are further from the linear fit (σ_S even increases when transitioning from a pixel-level scale of 120 to 60 m). This is most likely a statistical issue, where the four available subpixels are not sufficient to describe the actual subpixel reflectance distribution.

Linear regressions through the data in log-log space yield the relative susceptibilities S_{σ_V} , S_{cov} , and S_{σ_S} , which describe a relative change in the variability parameters σ_V , $\text{cov}(R_V, R_S)$, and σ_S with a relative change in pixel-level horizontal resolution, respectively (Feingold et al., 2001; Werner et al., 2014):

$$\begin{aligned} S_{\sigma_V} &= \frac{\text{scale}}{\sigma_V} \cdot \frac{d \sigma_V}{d \text{scale}} = \frac{d \ln \sigma_V}{d \ln \text{scale}} \\ S_{\text{cov}} &= \frac{\text{scale}}{\text{cov}(R_V, R_S)} \cdot \frac{d \text{cov}(R_V, R_S)}{d \text{scale}} = \frac{d \ln \text{cov}(R_V, R_S)}{d \ln \text{scale}} \\ S_{\sigma_S} &= \frac{\text{scale}}{\sigma_S} \cdot \frac{d \sigma_S}{d \text{scale}} = \frac{d \ln \sigma_S}{d \ln \text{scale}}. \end{aligned} \quad (5)$$

The linear regressions, which determine these susceptibility parameters, are indicated by gray diagonal lines in Figure 7. Due to the breakdown of the power law behavior for $\eta = 4$, the regression parameters were derived without this specific data point. There is a high correlation between observed data and the respective linear regressions, with correlation coefficients of $r > 0.92$. The relative susceptibilities are $S_{\sigma_V} = 0.383$, $S_{\text{cov}} = 0.691$ and $S_{\sigma_S} = 0.184$, which means that there is almost a factor of 2 between S_{cov} and S_{σ_V} , as well as S_{σ_V} and S_{σ_S} . However, even though $\text{cov}(R_V, R_S)$ is most susceptible to a change in pixel-level horizontal resolution, it is several orders of magnitude smaller than the respective σ_V and σ_S values.

While an increase in pixel-level scale yields an increase in subpixel variability, the opposite relation is observed for changes in subpixel scale. Figures 7d–7f show a logarithmic decrease in σ_V , $\text{cov}(R_V, R_S)$, and σ_S , which were derived from sampled subpixel reflectances at increasing horizontal resolutions between 30 and 960 m. Here the pixel-level scale is fixed at 1,920 m. Similar to the pixel-level relationships, there is a breakdown of the power law behavior for $\eta = 4$ (i.e., 960-m observations within a 1,920-m pixel). These observations are characterized by an increase in interquartile range and significant deviations from the linear regressions. Omitting this last data point from the regression analysis yields $r > 0.92$ and relative susceptibilities of $S_{\sigma_V} = 0.137$, $S_{\text{cov}} = 0.311$, and $S_{\sigma_S} = 0.107$. Again, $S_{\text{cov}} > S_{\sigma_V} > S_{\sigma_S}$, although the susceptibilities toward changes in subpixel scale are smaller than toward changes in pixel-level horizontal resolution.

5.2. PPHB Correction for Different Scales

The analysis in section 5.1 illustrates that elements of the subpixel variability vector $[\sigma_V^2, \text{cov}(R_V, R_S), \sigma_S^2]^T$ in equation (3) vary significantly, depending on the respective horizontal resolution of the subpixel and pixel-level observations. However, increased subpixel variabilities do not automatically imply an increase in magnitude of $\Delta\tau$ and Δr_{eff} . For one, the susceptibility parameters S_{σ_V} , S_{cov} , and S_{σ_S} exhibit the same sign. This is significant since the analysis in Figure 2 suggests that the sign of the second and third elements of the second-order derivative matrix is generally opposite to the sign of the first matrix element, which (at least partially) mitigates the impact of an increased or decreased subpixel variability on the PPHB. Moreover, the magnitude of $\Delta\tau$ and Δr_{eff} depends on the position of \bar{R}_V and \bar{R}_S within the LUT and thus the magnitude of the respective second-order derivatives. To study the impact of scale on the reliability of the PPHB predictions, the horizontal resolutions of both the subpixel and pixel-level ASTER observations are varied between 30 and 960 m. Subsequently, $\Delta\tau$ and Δr_{eff} are derived for each scale combination following equation (3) and compared to the actually observed results.

Figure 8a shows PDFs of the ratio $\tau(\bar{R}_V, \bar{R}_S)$ to $\tau(R_V, R_S)$, both with (blue) and without (black) a correction with calculated $\Delta\tau$, for subpixel ASTER observations with a horizontal resolution of 480 m and pixel-level data with a horizontal resolution of 960 m. This scenario means that both the VNIR and SWIR reflectances exhibit $\eta = 4$, which closely resembles measurements by the MODIS instrument. Similar to the results shown in Figure 6a for the 30 m subpixel resolution, the correction can successfully mitigate the mainly negative PPHB and for most observations the ratio is close to 1. This is also true for the correction of $r_{\text{eff}}(\bar{R}_V, \bar{R}_S)$ with calculated Δr_{eff} , which is shown in Figure 6b.

The correlation coefficient r between predicted and observed $\Delta\tau$ and Δr_{eff} for all combinations of subpixel and pixel-level horizontal resolutions is illustrated in Figure 8c. This analysis yields a multitude of combinations for most η values. As an example, $\eta = 64$ is achieved by 30-m subpixel data within 240-m pixels, 60-m data within 480-m pixels, and 120-m data within 960-m pixels. The white line in Figure 8c represents the mean r for each η value, enclosed by a shaded area indicating plus/minus one standard deviation. Because of the decreased correlation for low optical thickness $\tau(R_V, R_S) < 5$ (see section 4.2), both the $\Delta\tau$ results for the complete data

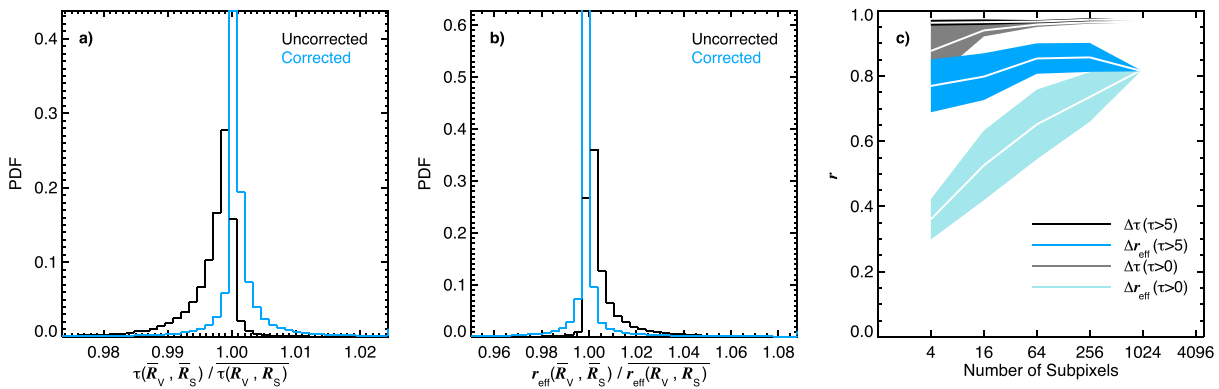


Figure 8. (a) Probability density function (PDFs) of the ratio of observed $\tau(\bar{R}_V, \bar{R}_S)$ to $\tau(R_V, R_S)$ (black) and the ratio of observed $\tau(\bar{R}_V, \bar{R}_S)$, which has been corrected by the predicted $\Delta\tau$ based on equation (3), to $\tau(R_V, R_S)$ (blue). Values have been derived from subpixel data with a horizontal resolution of 480 m and pixel-level data with a horizontal resolution of 960 m. (b) Same as (a) but for the effective droplet radius r_{eff} . (c) Pearson's product-moment correlation coefficient r for the correlation between observed and predicted $\Delta\tau$ and Δr_{eff} as a function of the number of available subpixels. White lines indicate the mean r for all possible combinations of subpixel and pixel-level horizontal resolution, while shaded areas indicate the mean plus/minus one standard deviation. The data set is separated into observations with $\tau(\bar{R}_V, \bar{R}_S), \tau(R_V, R_S) > 5$ (black and blue for $\Delta\tau$ and Δr_{eff} , respectively) and $\tau(\bar{R}_V, \bar{R}_S), \tau(R_V, R_S) > 0$ (gray and cyan for $\Delta\tau$ and Δr_{eff} , respectively).

set (gray) and for $\tau(R_V, R_S) > 5$ (black) are shown. Similarly, Δr_{eff} results from all pixels (cyan) and from pixels with $\tau(R_V, R_S) > 5$ (blue) are shown individually. For reasonably thick clouds mean correlation coefficients show only a weak dependence on η , with $r = 0.96 - 0.98$ for $\Delta\tau$ and $r = 0.77 - 0.87$ for Δr_{eff} . Especially for the $\Delta\tau$ correlations the standard deviations are very small, illustrating that all scale combinations for the respective η yield basically the same result. This illustrates that even if there is only a small number of available subpixels to calculate the variability vector $[\sigma_V^2, \text{cov}(R_V, R_S), \sigma_S^2]^T$ in equation (3), the predicted $\Delta\tau$ and Δr_{eff} still are a reliable estimate of the actually observed PPHB.

Including cloudy pixels with $\tau(R_V, R_S) < 5$ in the analysis barely changes the correlation coefficients for $\Delta\tau$, except for $\eta = 4$. Here the results show a larger spread (illustrated by the larger standard deviation) and a smaller mean $r = 0.88$ (a decrease of about 0.09). For thin clouds a much stronger dependence of r on η is found for Δr_{eff} . While for $\eta = 1,024$, correlation coefficients reach a similar value as for the data set with $\tau(R_V, R_S) > 5$, there is a significant decrease from $r = 0.82$ to $r = 0.36$ for $\eta = 4$. A similar behavior of $\Delta\tau$ and Δr_{eff} for decreasing η exists for the nRMSD. This dependence of r on η for thin clouds is mainly caused by the reduced retrieval sensitivity due to the convergence of the r_{eff} isolines in the LUT (see Figure 1 and the discussion in Zhang & Platnick, 2011; Werner et al., 2013). This behavior of the LUT yields substantially higher uncertainties in the retrievals of $r_{\text{eff}}(\bar{R}_V, \bar{R}_S)$ and $\bar{r}_{\text{eff}}(R_V, R_S)$ for low τ , which affects both the actually observed Δr_{eff} and the calculation of the matrix of second-order derivatives in equation (3). The effect of increased uncertainties in the derived matrix elements is further magnified because for thin clouds with $\tau(R_V, R_S) < 5$ there is considerable variability in the sign and value of each matrix element, as illustrated in Figures 2d and 2e, and even the covariance and cross-reflectance terms have a large contribution to Δr_{eff} . Conversely, uncertainty contributions from the truncation error in the derivation of equation (3) are found to be negligible. This was tested by calculating the relative third-order subpixel variabilities δ_V^3 and δ_S^3 , which are defined as follows:

$$\delta_V^3 = 100 \cdot \frac{\overline{\Delta R_{V,i}^3}}{\bar{R}_V} = 100 \cdot \frac{\frac{1}{n} \sum_{i=1}^n (R_{V,i} - \bar{R}_V)^3}{\bar{R}_V}$$

$$\delta_S^3 = 100 \cdot \frac{\overline{\Delta R_{S,i}^3}}{\bar{R}_S} = 100 \cdot \frac{\frac{1}{n} \sum_{i=1}^n (R_{S,i} - \bar{R}_S)^3}{\bar{R}_S}, \quad (6)$$

for both VNIR and SWIR reflectances. Both terms exhibit very low values in the range of 0.04–0.6%, regardless of the spatial resolution of the observations. Given these small contributions, it is not surprising that

predicted $\Delta\tau$ and Δr_{eff} , which are based on a form of equation (3) that includes third-order derivatives, yields indistinguishable results from the second-order PPHB predictions (not shown).

5.3. PPHB Correction With a Single High-Resolution Band

To evaluate the feasibility of a PPHB correction based on a single high-resolution reflectance band in the VNIR, the relative contributions of individual matrix elements to the overall PPHB are quantified for all 48 MBL cloud scenes. For the cloud optical thickness the individual contributions $\delta\tau_i$ (with $i = 1, 2, 3$ indicating the three respective matrix elements) to the total $\Delta\tau$ are defined as follows:

$$\begin{aligned}\delta\tau_1 &= 100 \cdot \frac{-\frac{1}{2} \frac{\partial^2 \tau(\bar{R}_V, \bar{R}_S)}{\partial^2 R_V} \bar{R}_V^{-2} \cdot H_{\sigma_V}^2}{\Delta\tau} \\ \delta\tau_2 &= 100 \cdot \frac{-\frac{\partial^2 \tau(\bar{R}_V, \bar{R}_S)}{\partial R_V \partial R_S} \bar{R}_V \bar{R}_S \cdot H_{\text{cov}}}{\Delta\tau} \\ \delta\tau_3 &= 100 \cdot \frac{-\frac{1}{2} \frac{\partial^2 \tau(\bar{R}_V, \bar{R}_S)}{\partial^2 R_S} \bar{R}_S^{-2} \cdot H_{\sigma_S}^2}{\Delta\tau}.\end{aligned}\quad (7)$$

In a similar way the relative contributions $\delta r_{\text{eff},i}$ are defined as follows:

$$\begin{aligned}\delta r_{\text{eff},1} &= 100 \cdot \frac{-\frac{1}{2} \frac{\partial^2 r_{\text{eff}}(\bar{R}_V, \bar{R}_S)}{\partial^2 R_V} \bar{R}_V^{-2} \cdot H_{\sigma_V}^2}{\Delta r_{\text{eff}}} \\ \delta r_{\text{eff},2} &= 100 \cdot \frac{-\frac{\partial^2 r_{\text{eff}}(\bar{R}_V, \bar{R}_S)}{\partial R_V \partial R_S} \bar{R}_V \bar{R}_S \cdot H_{\text{cov}}}{\Delta r_{\text{eff}}} \\ \delta r_{\text{eff},3} &= 100 \cdot \frac{-\frac{1}{2} \frac{\partial^2 r_{\text{eff}}(\bar{R}_V, \bar{R}_S)}{\partial^2 R_S} \bar{R}_S^{-2} \cdot H_{\sigma_S}^2}{\Delta r_{\text{eff}}}.\end{aligned}\quad (8)$$

Figure 9a shows PDFs of $\delta\tau_1$, $\delta\tau_2$, and $\delta\tau_3$, which are derived from all $n = 59,876$ overcast pixels that make up the statistical PPHB comparison in Figure 5. For the 48 MBL scenes most $\delta\tau_1$ are in the range of 80–130%, with a median value of 107%. This indicates a slight overestimation in predicted PPHB for most data points, if just the first matrix element is used to derive $\Delta\tau$. Both $\delta\tau_2$ and $\delta\tau_3$ have mostly negligible contributions, with median values of –6% and –1%, respectively. The negative sign indicates that the second and third matrix elements have a mostly positive sign, whereas the total PPHB for the cloud optical thickness is almost exclusively negative (see Figure 5a). The illustrated importance of the first matrix element to the overall negative τ bias confirms the findings in Figures 2a–2c. In this example LUT the first matrix element yields the main contribution to the overall $\Delta\tau$, except for very large τ .

Figure 9b shows the PDFs of $\delta r_{\text{eff},1}$, $\delta r_{\text{eff},2}$, and $\delta r_{\text{eff},3}$ for the same $n = 59,876$ overcast pixels. As predicted in Figures 2d–2f, all three matrix elements have a sizeable impact on Δr_{eff} , with median values of 161%, 16%, and –89% for the first, second, and third matrix element, respectively. Similar to $\delta\tau_1$, $\delta r_{\text{eff},1}$ has the same sign as the overall PPHB, while exceeding 100%. Conversely, $\delta r_{\text{eff},2}$ is centered around 0% and $\delta r_{\text{eff},3}$ is highly negative.

To understand the combination of individual elements better, a joint PDF of $\delta r_{\text{eff},1}$ and $\delta r_{\text{eff},2}$ is shown in Figure 9c. It is obvious that the second matrix element is usually much smaller than the first. The few pixels with larger $\delta r_{\text{eff},2}$ contributions are characterized by comparable $\delta r_{\text{eff},1}$. There is a thin stripe of negative $\delta r_{\text{eff},1}$, which is associated with very low effective droplet radius observations. A similar thin stripe is apparent in Figure 2d, right at the upper boundary of the LUT. In this region the LUT starts to overlap with itself and the r_{eff} retrievals become ambiguous. As a result, the predicted PPHB for these pixels is not very reliable. A similar joint PDF of $\delta r_{\text{eff},1}$ and $\delta r_{\text{eff},3}$ is shown in Figure 9d. For most observations, $\delta r_{\text{eff},1}$ is about twice as large as the absolute value of $\delta r_{\text{eff},3}$. Again, a thin stripe of highly positive (negative) $\delta r_{\text{eff},1}$ ($\delta r_{\text{eff},3}$) is visible in the upper right quadrant, associated with the multiple-solution space in the LUT (see Figures 2e and 2f). The distribution of $\delta r_{\text{eff},i}$ illustrates that a prediction based on just the first matrix element in equation (3) yields an overestimated Δr_{eff} . However, these results are still useful as an estimate of the upper PPHB limit for r_{eff} .

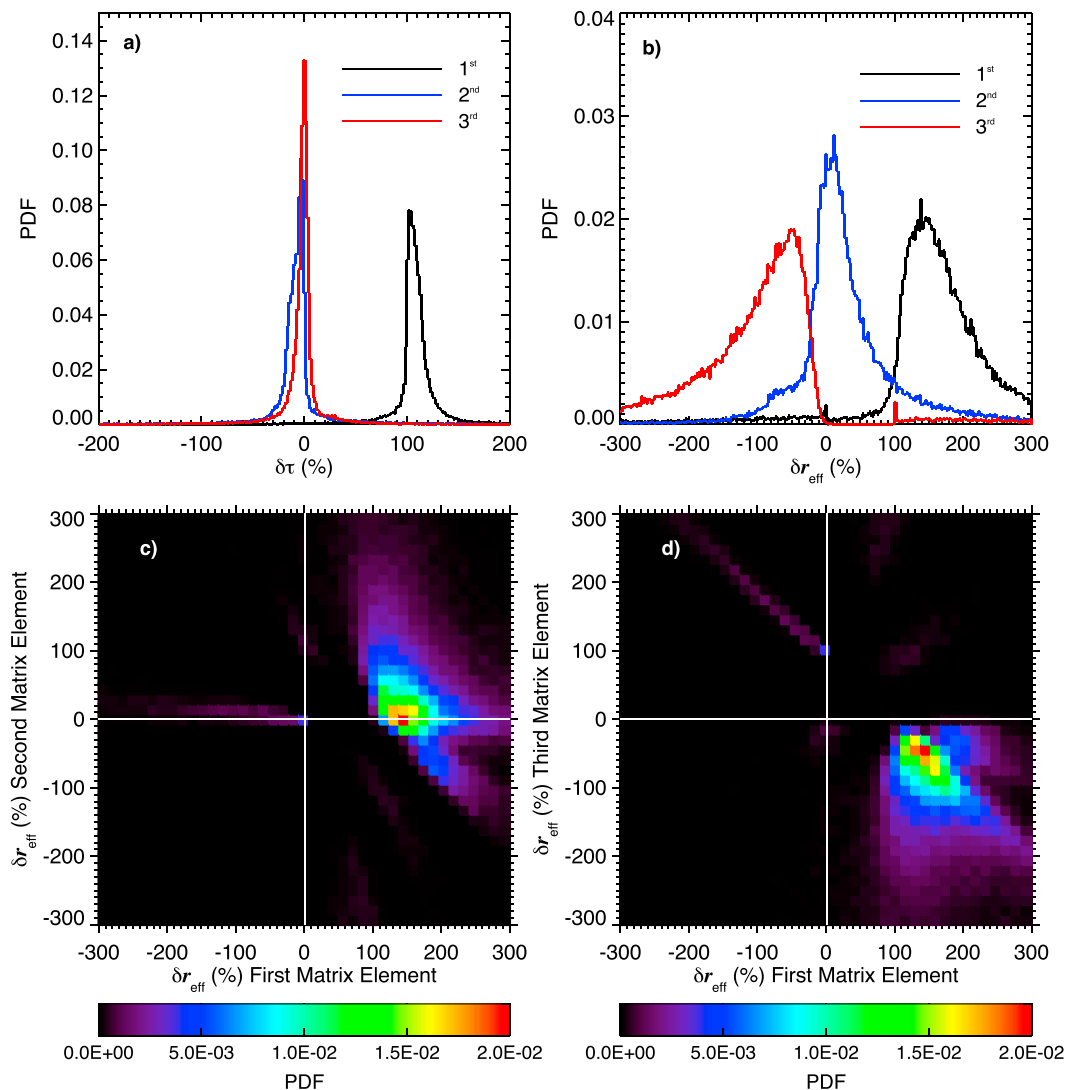


Figure 9. (a) Probability density function (PDF) of the relative contributions $\delta\tau_i$ of the first ($i = 1$, black), second ($i = 2$, blue), and third ($i = 3$, red) matrix elements to the overall plane-parallel homogeneous bias $\Delta\tau$. Data are from 48 marine boundary layer scenes sampled by Advanced Spaceborne Thermal Emission and Reflection Radiometer off the coast of California. (b) Same as (a) but for the effective droplet radius bias Δr_{eff} . (c) PDF of the first and second matrix element contributions $\delta r_{\text{eff}, 1}$ and $\delta r_{\text{eff}, 2}$. (d) Same as (c) but for the first and third matrix element contributions $\delta r_{\text{eff}, 1}$ and $\delta r_{\text{eff}, 3}$.

The correlation between observed and predicted PPHB, based on only the first matrix elements in equation (3), is shown in Figures 10a and 10b for $\Delta\tau$ and Δr_{eff} , respectively. The number of overcast pixels in the analysis is slightly increased, from $n = 59,876$ in Figure 5 to $n = 60,943$, because only the first matrix element needs to be derived successfully. When calculating the complete PPHB based on all elements the calculation of the second (cross-correlation) terms $-\frac{\partial^2\tau(\bar{R}_V, \bar{R}_S)}{\partial R_V \partial R_S}$ and $-\frac{\partial^2 r_{\text{eff}}(\bar{R}_V, \bar{R}_S)}{\partial R_V \partial R_S}$ can fail at the edge of the LUT, because a higher number of step points are necessary to calculate the mixed numerical derivatives and there is a higher chance of points falling outside the solution space. There is still a high correlation between observed and predicted $\Delta\tau$ with $r = 0.98$, while the nRMSD slightly increases from 0.25% to 0.29%. Figure 10c shows the results of a correction of the pixel-level retrievals with these new $\Delta\tau$ values. Here similar to Figure 6c, PDFs of the ratio of corrected and uncorrected $\tau(\bar{R}_V, \bar{R}_S)$ to $\tau(R_V, R_S)$ are shown. There is a close agreement between the fully corrected results (blue), which use all three matrix elements, and the ones using only the first matrix element (red). A slight overestimation in the magnitude of predicted $\Delta\tau$, already indicated by the PDF in Figure 9a, is visible and as a result the corrected pixel-level retrievals are slightly larger than the ones from the correction with all three matrix elements. Similar results are achieved for Δr_{eff} , as shown in Figure 10b.

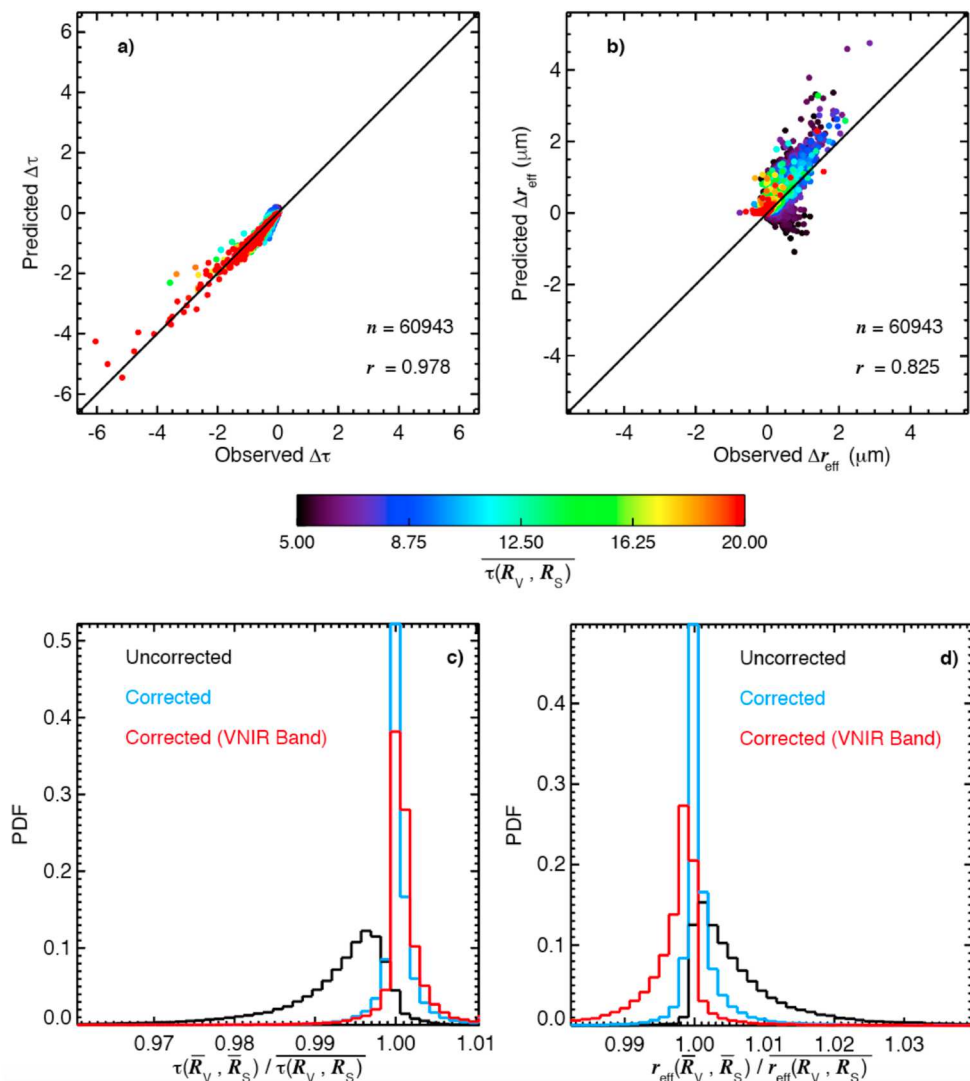


Figure 10. (a) Scatter plot of observed versus predicted plane-parallel homogeneous bias for the cloud optical thickness τ , derived from subpixel data with a horizontal resolution of 30 m and pixel-level data with a horizontal resolution of 960 m. The prediction is only based on the first matrix element, shown in Figure 2a. Data are from 48 marine boundary layer scenes sampled off the coast of California, amounting to $n = 60,943$ pixels with a subpixel cloud cover $C_{\text{sub}} = 1$. Colors indicate the respective pixel value of $\tau(R_V, R_S)$. (b) Same as (a) but for the effective droplet radius r_{eff} . The prediction is only based on the first matrix element, shown in Figure 2d. (c) Probability density function (PDF) of the ratio of observed $\tau(\bar{R}_V, \bar{R}_S)$ (uncorrected in black, corrected with the full matrix in blue, corrected with only the first matrix element in red) to $\tau(R_V, R_S)$. (d) Same as (c) but for r_{eff} . VNIR indicates the visible to near-infrared spectral wavelength range.

Here the predicted PPHB is slightly higher than the observed one, especially for small $\tau(R_V, R_S)$, and $\text{nRMSD} = 1.19\%$ (up from $\text{nRMSD} = 0.87\%$). However, the correlation coefficient is comparable to the prediction based on all three matrix elements and equation (3) yields a reliable estimate of Δr_{eff} , which can be interpreted as the upper limit of the PPHB. This indicates that there are pixels where a correction of $r_{\text{eff}}(\bar{R}_V, \bar{R}_S)$ with the new Δr_{eff} values yields results that are slightly lower than the respective $\bar{r}_{\text{eff}}(R_V, R_S)$ (i.e., an overestimation of the PPHB). However, as shown in Figure 10d, this overestimation of Δr_{eff} yields pixel-level retrievals that are still closer to the mean subpixel results than the uncorrected ones. Not only is the percentage of observations with a ratio of 1 higher, the maximum deviations are also smaller than for the uncorrected results. Because ΔLWP is determined by both $\Delta \tau$ and Δr_{eff} , all three matrix elements are important in determining the PPHB for the LWP . Similar to Δr_{eff} , the first matrix element alone yields an overestimation of the actually observed PPHB.

There is a reduced correlation of $r = 0.662$ between ΔLWP from only a single band and the full correction matrix. However, despite using only the first matrix element, the median ratio of corrected pixel-level to mean subpixel LWP is 0.999.

6. Summary and Discussion

This study provides experimental validation and further evaluation of the mathematical framework introduced in Z16, which expands the subpixel τ and r_{eff} retrievals into two-dimensional Taylor series of cloud-top reflectances. This method decomposes the contributions from the retrieval sensitivity, determined by the shape of the LUT, and from the subpixel reflectance variability to the sign and magnitude of the PPHB. The framework is tested with ASTER observations at horizontal scales between 30 and 1,920 m sampled over 48 MBL cloud scenes with varying degrees of heterogeneity.

ASTER cloud-top reflectances R_V and R_S sampled at 30 m are used to retrieve high-resolution τ and r_{eff} , which subsequently yield the mean values of the subpixel results $\tau(R_V, R_S)$ and $\overline{r_{\text{eff}}}(R_V, R_S)$. R_V and R_S samples are aggregated to a horizontal resolution of 960 m and provide the pixel-level retrievals $\tau(\overline{R_V}, \overline{R_S})$ and $\overline{r_{\text{eff}}}(\overline{R_V}, \overline{R_S})$. The difference between the pixel-level and mean high-resolution results yields the observed PPHB, which reaches values of up to -6.05 and $2.86 \mu\text{m}$ for $\Delta\tau$ and Δr_{eff} , respectively. For all analyzed pixels, the 1st percentile of observed $\Delta\tau$ is -4.0% , while the 99th percentile of observed Δr_{eff} is $+4.7\%$. Compared to the retrieval uncertainties the observed PPHB is about 27% ($\Delta\tau$) and 20% (Δr_{eff}) in magnitude. While the impact of the PPHB seems small in comparison, it is important to note that both $\Delta\tau$ and Δr_{eff} represent a bias that systematically affects the cloud property retrievals, independent from the retrieval uncertainty.

A comparison between the observed $\Delta\tau$ and Δr_{eff} and predicted PPHB based on the framework introduced in Z16 reveals a good agreement, with correlation coefficients of $r > 0.97$ for $\Delta\tau$ and $r > 0.79$ for Δr_{eff} . Similar results are found for the bias in LWP (ΔLWP), which can be derived as the product of τ and r_{eff} . For all analyzed pixels $-20.90 \text{ g m}^2 < \Delta LWP < 10.96 \text{ g m}^2$, while the correlation between observed and predicted ΔLWP is $r = 0.86$. However, no systematic low or high PPHB is found for the LWP . A correction of the retrievals based on aggregated reflectances with predicted $\Delta\tau$, Δr_{eff} , and ΔLWP mitigates the observed PPHB and yields a closer agreement between the pixel-level results and the mean values of the subpixel retrievals.

The reliability of the PPHB prediction is studied for the following: (i) varying horizontal resolutions of subpixel and pixel-level observations, which determines the number of available pixels η to calculate the subpixel reflectance variability; (ii) a limited mathematical framework with reflectances from only a single high-resolution band in the VNIR. Analysis (i) is necessary, because it is found that an increase in pixel-level (subpixel) horizontal resolution yields an increase (decrease) in subpixel reflectance variability, which together with the LUT shape determine the sign and magnitude of the PPHB. While no dependence of r on η is found for pixels with $\tau(R_V, R_S) > 5$, a reduction of r for Δr_{eff} exists for pixels with low optical thickness. The increased uncertainty in the Δr_{eff} prediction can be explained by an increased retrieval uncertainty due to the shape of the LUT, which impacts $r_{\text{eff}}(\overline{R_V}, \overline{R_S})$ and $\overline{r_{\text{eff}}}(R_V, R_S)$, as well as the distribution of the numerical derivatives in the Taylor series within the LUT. In contrast, contributions from higher-order terms, which are ignored in the Taylor expansion of τ and r_{eff} , are found to be negligible. Analysis (ii), meanwhile, is important because not all satellite-borne imagers provide high-resolution samples in the respective SWIR band. PPHB predictions based on just the VNIR band contributions show a slight overestimation of the observed PPHB, but overall, there is a good agreement between predicted and observed $\Delta\tau$, Δr_{eff} , and ΔLWP . The fact that even limited observations of the subpixel reflectance variability are sufficient to mitigate the PPHB in pixel-level retrievals has important implications for the common satellite missions that provide operational cloud retrievals, such as MODIS, VIIRS, and SEVIRI. It can also guide the instrument design for future satellite missions.

Further studies will help to improve the predictions of $\Delta\tau$ and Δr_{eff} . An expansion of the analysis from 48 MBL scenes to hundreds of scenes is planned in the near future. This larger data set will allow for better statistics, as well as the opportunity to study the PPHB for different cloud types, environmental conditions, and viewing geometries. Including higher-order terms in the Taylor expansion of τ and r_{eff} might provide even more reliable PPHB estimates. However, numerical approximations of higher-order derivatives not only require a high-resolution LUT; the increased number of step points in the numerical derivation proves problematic at the edge of the LUT. The mathematical framework to predict the PPHB can also be expanded to the retrievals of cirrus cloud properties, which are usually derived by the split-window technique

(Inoue, 1985; Parol et al., 1991). Here variabilities in the applied brightness temperatures are likewise inducing uncertainties in the retrieved cirrus variables (Fauchez et al., 2015), which requires a Taylor expansion by means of thermal infrared observations and the analysis of second-order derivatives in completely different LUTs.

Finally, it is important to note that the framework presented in Z16 and this study merely provides the means to reliably derive pixel-level retrievals that are in close agreement with the mean high-resolution subpixel τ and r_{eff} retrievals. The possible impact of 3-D radiative effects due to resolved variability (e.g., cloud shadows, illuminated cloud sides, photon leaking, and radiative smoothing and scale breaks) might induce a reflectance variability that is wrongfully attributed to changes in the underlying cloud properties. In these circumstances, the mean high-resolution subpixel retrievals might not be representative of the true cloud properties. Following the discussion in Zhang et al. (2012), Z16, and this study, the pixel-level τ and r_{eff} retrievals based on IPA are predominantly smaller and larger than the mean subpixel properties, respectively. However, 3-D radiative effects can impact higher-resolution retrievals and introduce significant biases to the true cloud variables. As reported by Varnai and Marshak (2001, 2002) and Marshak et al. (2006), the sign and magnitude of these biases are dependent on the solar geometry, cloud brightness, and the distribution of shadowed and illuminated cloud elements within a scene, among others. Using a number of assumptions, these studies conclude that 3-D radiative effects induce a net overestimation in both τ and r_{eff} , while the bias for individual cloud elements can exhibit opposite signs and widely varying magnitudes. If both 3-D effects and the PPHB have a positive sign, mitigating Δr_{eff} by means of equation (3) potentially yields results that are closer to the true r_{eff} . Conversely, negative $\Delta \tau$ and positive biases from 3-D radiative effects might (at least to a degree) offset each other. In this case, the uncorrected pixel-level τ retrievals might be good estimates of the true cloud properties. While the focus of this study is on the PPHB, a future study aims at applying the methods described in Varnai and Marshak (2002) to ASTER data to study biases for high-resolution remote sensing observations. However, to truly quantify the relative contributions of PPHB and 3-D radiative effects, a ground truth is necessary (i.e., knowledge of the true subpixel cloud properties), which could be achieved by future studies applying a combination of large eddy simulations and both 1-D and 3-D radiative transfer solvers.

Acknowledgments

This study is supported by NASA grants NNX14AJ25G and NNX15AC77G. The hardware used in the computational studies is part of the UMBC High Performance Computing Facility (HPCF). The facility is supported by the U.S. National Science Foundation through the MRI program (grants CNS-0821258 and CNS-1228778) and the SCREMS program (grant DMS-0821311), with additional substantial support from the University of Maryland, Baltimore County (UMBC). ASTER data are obtained by the EarthExplorer interface (<http://earthexplorer.usgs.gov>) provided by the U.S. Geological Survey (USGS). ASTER cloud property retrievals are based on a research-level retrieval algorithm and a publicly available, quality-assured product is in preparation. In the meantime, we have a preliminary data set of cloud-top, optical, and microphysical properties, as well as cloud masking information, for several hundred marine stratocumulus and broken cumulus scenes sampled by ASTER (Werner et al., 2016; Zhao et al., 2009). We are happy to share these products with the community and encourage anybody interested in the data, which are available in HDF4 format, to contact us (either frankw@umbc.edu or zzbatmos@umbc.edu).

References

Abrams, M. (2000). The Advanced Spaceborne Thermal Emission and Reflection Radiometer (ASTER): Data products for the high spatial resolution imager on NASA's Terra platform. *International Journal of Remote Sensing*, 21(5), 847–859.

Abrams, M., Hook, S., & Ramachandran, B. (2004). ASTER User Handbook Version 2: Jet Propulsion Laboratory, California Institute of Technology, 4800 Oak Grove Dr., Pasadena, CA 91109.

Barker, H., & Liu, D. (1995). Inferring optical depth of broken clouds from Landsat data. *Journal of Climate*, 8, 2620–2630.

Cahalan, R., & Joseph, J. (1989). Fractal statistics of cloud fields. *Monthly Weather Review*, 117, 261–272.

Cahalan, R., Ridgway, W., Wiscombe, W., & Bell, T. (1994). The albedo of fractal stratocumulus clouds. *Journal of the Atmospheric Sciences*, 51, 2434–2455.

Cahalan, R., Ridgway, W., Wiscombe, W., & Gollmer, S. (1994). Harshvardhan Independent pixel and Monte Carlo estimates of stratocumulus albedo. *Journal of the Atmospheric Sciences*, 51, 3776–3790.

Chambers, L., Wielicki, B., & Evans, K. (1997). Accuracy of the independent pixel approximation for satellite estimates of oceanic boundary layer cloud optical depth. *Journal of Geophysical Research*, 102(D2), 1779–1794.

Cho, H.-M., Zhang, Z., Meyer, K., Lebsack, M., Platnick, S., Ackerman, A. S., et al. (2015). Frequency and causes of failed MODIS cloud property retrievals for liquid phase clouds over global oceans. *Journal of Geophysical Research: Atmospheres*, 120, 4132–4154. <https://doi.org/10.1002/2015JD023161>

Coakley, J. A., Jr., Friedman, M. A., & Tahnk, W. R. (2005). Retrieval of cloud properties for partly cloudy imager pixels. *Journal of Atmospheric and Oceanic Technology*, 22(1), 3–17. <https://doi.org/10.1175/JTECH-1681.1>

Davis, A., Marshak, A., Cahalan, R., & Wiscombe, W. (1997). The Landsat scale break in stratocumulus as a three-dimensional radiative transfer effect: Implications for cloud remote sensing. *Journal of the Atmospheric Sciences*, 54(2), 241–260.

Davis, A. B., & Marshak, A. (2010). Solar radiation transport in the cloudy atmosphere: A 3D perspective on observations and climate impacts. *Reports On Progress In Physics*, 73(2), 26801. <https://doi.org/10.1088/0034-4885/73/2/026801>

Di Girolamo, L., Liang, L., & Platnick, S. (2010). A global view of one-dimensional solar radiative transfer through oceanic water clouds. *Geophysical Research Letters*, 37, L18809. <https://doi.org/10.1029/2010GL044094>

Fauchez, T., Dubuisson, P., Cornet, C., Szczap, F., Garnier, A., Pelon, J., & Meyer, K. (2015). Impacts of cloud heterogeneities on cirrus optical properties retrieved from space-based thermal infrared radiometry. *Atmospheric Measurement Techniques*, 8(2), 633–647. <https://doi.org/10.5194/amt-8-633-2015>

Feingold, G., Remer, L., Ramaprasad, J., & Kaufman, Y. (2001). Analysis of smoke impact on clouds in Brazilian biomass burning regions: An extension of Twomey's approach. *Journal of Geophysical Research*, 106(D19), 22,907–22,922.

Han, Q., Rossow, W., & Lacis, A. (1994). Near-global survey of effective droplet radii in liquid water clouds using ISCCP data. *Journal of Climate*, 7, 465–497.

Inoue, T. (1985). On the temperature and effective emissivity determination of semi-transparent cirrus clouds by bi-spectral measurements in the 10 μm window region. *Journal of the Meteorological Society of Japan. Ser. II*, 63(1), 88–99.

Jiang, J. H., Su, H., Zhai, C., Perun, V. S., Del Genio, A., Nazarenko, L. S., et al. (2012). Evaluation of cloud and water vapor simulations in CMIP5 climate models using NASA "A-Train" satellite observations. *Journal of Geophysical Research: Atmospheres*, 117, D14105. <https://doi.org/10.1029/2011JD017237>

King, M., Tsay, S.-C., Platnick, S., Wang, M., & Liou, K.-N. (1997). Cloud retrieval algorithms for MODIS: Optical thickness, effective particle radius, and thermodynamic phase. *Tech. Rep.*, NASA Goddard Space Flight Center.

Lee, T. E., Miller, S. D., Turk, F. J., Schueler, C., Julian, R., Deyo, S., et al. (2006). The NPOESS VIIRS day/night visible sensor. *Bulletin of the American*, 87(2), 191–199. <https://doi.org/10.1175/BAMS-87-2-191>

Liang, L., Di Girolamo, L., & Sun, W. (2015). Bias in MODIS cloud drop effective radius for oceanic water clouds as deduced from optical thickness variability across scattering angles. *Journal of Geophysical Research: Atmospheres*, 120, 7661–7681. <https://doi.org/10.1002/2015JD023256>

Liang, L. S., Di Girolamo, L., & Platnick, S. (2009). View-angle consistency in reflectance, optical thickness and spherical albedo of marine water-clouds over the northeastern Pacific through MISR-MODIS fusion. *Geophysical Research Letters*, 36, L09811. <https://doi.org/10.1029/2008GL037124>

Marshak, A., Davis, A., Wiscombe, W., & Cahalan, R. (1995). Radiative smoothing in fractal clouds. *Journal of Geophysical Research*, 100(D12), 26,247–26,261.

Marshak, A., Platnick, S., Varnai, T., Wen, G. Y., & Cahalan, R. F. (2006). Impact of three-dimensional radiative effects on satellite retrievals of cloud droplet sizes. *Journal of Geophysical Research*, 111(D9), D09207. <https://doi.org/10.1029/2005JD006686>

Miller, D. J., Zhang, Z., Ackerman, A. S., Platnick, S., & Baum, B. A. (2016). The impact of cloud vertical profile on liquid water path retrieval based on the bispectral method: A theoretical study based on large-eddy simulations of shallow marine boundary layer clouds. *Journal of Geophysical Research*, 121(8), 4122–4141. <https://doi.org/10.1002/2015JD024322>

Nakajima, T., & King, M. (1990). Determination of the optical thickness and effective particle radius of clouds from reflected solar radiation measurements. Part I: Theory. *Journal of the Atmospheric Sciences*, 47, 1878–1893.

Nakajima, T., King, M., Spinharne, J., & Radke, L. (1991). Determination of the optical thickness and effective particle radius of clouds from reflected solar radiation measurements. Part II: Marine stratocumulus observations. *Journal of the Atmospheric Sciences*, 48, 728–750.

Oreopoulos, L., Marshak, A., Cahalan, R., & Wen, G. (2000). Cloud three-dimensional effects evidenced in Landsat spatial power spectra and autocorrelation functions. *Journal of Geophysical Research*, 105(D11), 14,777–14,788.

Painemal, D., & Zuidema, P. (2011). Assessment of MODIS cloud effective radius and optical thickness retrievals over the Southeast Pacific with VOCALS-REx in situ measurements. *Journal of Geophysical Research*, 116, D24206.

Parol, F., Buriez, J. C., Brogniez, G., & Fouquart, Y. (1991). Information content of AVHRR channels 4 and 5 with respect to the effective radius of cirrus cloud particles. *Journal of Applied Meteorology*, 30(7), 973–984. <https://doi.org/10.1175/1520-0450-30.7.973>

Platnick, S., King, M., Ackerman, S., Menzel, W., Baum, B., Riedi, J., & Frey, R. (2003). The MODIS cloud products: Algorithms and examples from Terra. *IEEE Transactions on Geoscience and Remote Sensing*, 41, 459–473.

Roebeling, R., Feijt, A., & Stammes, P. (2006). Cloud property retrievals for climate monitoring: Implications of differences between Spinning Enhanced Visible and Infrared Imager (SEVIRI) on METEOSAT-8 and Advanced Very High Resolution Radiometer (AVHRR) on NOAA-17. *Journal of Geophysical Research*, 111, D20210. <https://doi.org/10.1029/2005JD006990>

Twomey, S., & Seton, K. J. (1980). Inferences of gross microphysical properties of clouds from spectral reflectance measurements. *Journal of the Atmospheric Sciences*, 37(5), 1065–1069.

Varnai, T., & Marshak, A. (2001). Statistical analysis of the uncertainties in cloud optical depth retrievals caused by three-dimensional radiative effects. *Journal of the Atmospheric Sciences*, 58, 1540–1548.

Varnai, T., & Marshak, A. (2002). Observations of the three-dimensional radiative effects that influence MODIS cloud optical thickness retrievals. *Journal of the Atmospheric Sciences*, 59, 1607–1618.

Walther, A., Heidinger, A. K., & Miller, S. (2013). The expected performance of cloud optical and microphysical properties derived from Suomi NPP VIIRS day/night band lunar reflectance. *Journal of Geophysical Research*, 118(23), 13,230–13,240. <https://doi.org/10.1002/2013JD020478>

Werner, F., Siebert, H., Pilewskie, P., Schmeissner, T., Shaw, R. A., & Wendisch, M. (2013). New airborne retrieval approach for trade wind cumulus properties under overlying cirrus. *Journal of Geophysical Research: Atmospheres*, 118(9), 3634–3649. <https://doi.org/10.1002/jgrd.50334>

Werner, F., Ditas, F., Siebert, H., Simmel, M., Wehner, B., Pilewskie, P., et al. (2014). Twomey effect observed from collocated microphysical and remote sensing measurements over shallow cumulus. *Journal of Geophysical Research: Atmospheres*, 119(3), 1534–1545. <https://doi.org/10.1002/2013JD020131>

Werner, F., Wind, G., Zhang, Z., Platnick, S., Di Girolamo, L., Zhao, G., et al. (2016). Marine boundary layer cloud property retrievals from high-resolution ASTER observations: Case studies and comparison with Terra MODIS. *Atmospheric Measurement Techniques*, 9(12), 5869–5894. <https://doi.org/10.5194/amt-9-5869-2016>

Wood, R., Jensen, M. P., Wang, J., Bretherton, C. S., Burrows, S. M., Genio, A. D. D., et al. (2016). Planning the next decade of coordinated research to better understand and simulate marine low clouds. *Bulletin of the American*, 97(9), 1699–1702. <https://doi.org/10.1175/BAMS-D-16-0160.1>

Yamaguchi, Y., & Hiroji, T. (1993). Scientific basis of ASTER instrument design. *SPIE*, 1939, 150–160. <https://doi.org/10.1117/12.152841>

Yamaguchi, Y., Kahle, A., Tsu, H., Kawakami, T., & Pniel, M. (1998). Overview of Advanced Spaceborne Thermal Emission and Reflection Radiometer (ASTER). *IEEE Transactions on Geoscience and Remote Sensing*, 36, 1062–1071.

Zhang, Z., & Platnick, S. (2011). An assessment of differences between cloud effective particle radius retrievals for marine water clouds from three MODIS spectral bands. *Journal of Geophysical Research*, 116(D20), D20215. <https://doi.org/10.1029/2011JD016216>

Zhang, Z., Ackerman, A. S., Feingold, G., Platnick, S., Pincus, R., & Xue, H. (2012). Effects of cloud horizontal inhomogeneity and drizzle on remote sensing of cloud droplet effective radius: Case studies based on large-eddy simulations. *Journal of Geophysical Research*, 117, D19208.

Zhang, Z., Werner, F., Cho, H.-M., Wind, G., Platnick, S., Ackerman, A. S., et al. (2016). A framework based on 2-D Taylor expansion for quantifying the impacts of subpixel reflectance variance and covariance on cloud optical thickness and effective radius retrievals based on the bispectral method. *Journal of Geophysical Research: Atmospheres*, 121, 7007–7025. <https://doi.org/10.1002/2016JD024837>

Zhao, G., Di Girolamo, L., Dey, S., Jones, A. L., & Bull, M. (2009). Examination of direct cumulus contamination on MISR-retrieved aerosol optical depth and angstrom coefficient over ocean. *Geophysical Research Letters*, 36, L13811. <https://doi.org/10.1029/2009GL038549>